Research Square

Preprints are preliminary reports that have not undergone peer review.
They should not be considered conclusive, used to inform clinical practice,
or referenced by the media as validated information.

Structural Mechanism and Regulation of the Phospholipid Methylase Cho2

Dianfan Li

lidf9@mail.sysu.edu.cn

School of Agriculture and Biotechnology, Sun Yat-sen University https://orcid.org/0000-0003-4729-4678

Tingting Li

School of Agriculture and Biotechnology, Sun Yat-sen University

Hao Xia

State Key Laboratory of Molecular Biology, Shanghai Institute of Biochemistry and Cell Biology, Center for Excellence in Molecule Cell Science, Chinese Academy of Sciences

Yulin Chao

Shanghai Stomatological Hospital, School of Stomatology, Shanghai Key Laboratory of Medical Epigenetics, International Co-laboratory of Medical Epigenetics and Metabolism, Fudan University

Yaning Li

School of Agriculture and Biotechnology, Sun Yat-sen University

Zixuan Zhou

Shanghai Stomatological Hospital, School of Stomatology, Shanghai Key Laboratory of Medical Epigenetics, International Co-laboratory of Medical Epigenetics and Metabolism, Fudan University

Zhihao Yue

School of Agriculture and Biotechnology, Sun Yat-sen University

Qianhui Qu

Fudan University https://orcid.org/0000-0002-5753-2599

Article

Keywords:

Posted Date: November 3rd, 2026

DOI: https://doi.org/10.21203/rs.3.rs-11448634/v1

License: This work is licensed under a Creative Commons Attribution 4.0 International License.
Read Full License

Additional Declarations: There is **NO** Competing Interest.

Title: Structural Mechanism and Regulation of the Phospholipid Methylase Cho2

Authors: Tingting Li[1,†], Hao Xia[2,†], Yulin Chao[†,3], Yaning Li[1], Zixuan Zhou[3], Zhihao Yue[1], Qianhui Qu[3,*], Dianfan Li[1,*]

Affiliation:

[1]School of Agriculture and Biotechnology, Sun Yat-sen University, Shenzhen, 518107, China.

[2]Center for Excellence in Molecular Cell Science, Shanghai Institute of Biochemistry and Cell Biology, University of CAS, Chinese Academy of Sciences (CAS), 320 Yueyang Road, Shanghai 200031, China.

[3] Eye & ENT Hospital, Institutes of Biomedical Sciences，Shanghai Key Laboratory of Medical Epigenetics, International Co-laboratory of Medical Epigenetics and Metabolism (Ministry of Science and Technology), Department of Systems Biology for Medicine, Fudan University, Shanghai 200032, China.

[†]Equal contribution. [*]Correspondence: qqh@fudan.edu.cn; lidf9@mail.sysu.edu.cn

ABSTRACT

Phosphatidylethanolamine (PE) methylation is a conserved eukaryotic pathway that maintains phospholipid homeostasis and influences diverse methylation-dependent processes by regulating the phosphatidylethanolamine/phosphatidylcholine (PE/PC) ratio and cellular methylation capacity. In fungi, the first and rate-limiting step of this pathway is catalyzed by Cho2, an unusual membrane methyltransferase containing two pseudo-symmetrical catalytic domains and a C-terminal soluble domain (C^{Sol}). Here, we report four cryo-electron microscopy structures of fungal Cho2 at 3.26–2.56 Å resolution, revealing an elongated homodimer in which each protomer contains two homologous six-transmembrane catalytic domains. The structures define the molecular basis for phospholipid recognition and reveal a mechanism for feedback inhibition by phosphatidylcholine. Biochemical analyses further show that the two catalytic domains are functionally coupled, while structural modeling identifies a communication helix that likely coordinates conformational changes associated with cofactor binding and catalysis. In addition, analyses of a C^{Sol}-truncation mutant and an inhibitory nanobody demonstrate that the C^{Sol} domain positively regulates enzymatic activity by promoting SAM binding. Together, these findings establish the molecular basis of Cho2 function and uncover multiple regulatory mechanisms governing the first committed step of fungal PE methylation.

INTRODUCTION

Phospholipid homeostasis is crucial for membrane integrity, membrane protein function, regulating lipid metabolism, energy production (reviewed in ref.[1,2]), endoplasmic reticulum (ER) homeostasis[3], autophagy[4,5], and epigenetic regulation[6,7]. A major determinant of phospholipid homeostasis in eukaryotic cells is the balance between phosphatidylcholine (PC) and phosphatidylethanolamine (PE), the two most abundant membrane phospholipids. PE is converted to PC through three sequential *S*-adenosyl methionine (SAM)-dependent methylation reactions that generate *S*-adenosyl homocysteine (SAH). By controlling both the cellular PE/PC ratio and SAM consumption, PE methylation links phospholipid metabolism to one-carbon metabolism and thereby influences a wide range of physiological processes[1]. Consistent with this central role, dysregulated PE methylation has been linked to metabolic disorders[8-15] including fatty liver disease, obesity, diabetes, and cancer in mammals, while disruption of the pathway in yeast results in choline auxotrophy and widespread defects in membrane homeostasis[16].

In budding yeast, PE methylation is the major route of PC biosynthesis and is catalyzed by two endoplasmic reticulum membrane methyltransferases[17]. Cho2 catalyzes the first and rate-limiting methylation of PE to phosphatidyl-*N*-monomethylethanolamine (PMME), whereas Opi3 catalyzes the subsequent two methylation reactions[18-21]. Because Cho2 catalyzes the committed step of the pathway, it has a broad impact on cellular physiology. Loss of Cho2 activity disrupts membrane lipid composition[22], induces ER stress[23] and unfolded protein responses[24,25], impairs autophagy[4,5,26] and glycosylphosphatidylinositol-anchor biogenesis[26], alters neutral lipid metabolism [27,28], and affects diverse methylation-dependent pathways by changing the cellular SAM/SAH ratio[6,29-31]. Defects in PE methylation also sensitize fungal cells to antifungal agents[32,33], highlighting the pathway as a potential therapeutic target.

Despite catalyzing the same class of SAM-dependent phospholipid methylation reactions, Cho2 differs strikingly from other membrane PE methyltransferases (PEMT).

Whereas Opi3 and mammalian PEMT are compact membrane proteins of approximately 20 kDa[34,35], Cho2 is an unusually large (~100 kDa) membrane protein containing two internally homologous catalytic domains embedded within the membrane together with a substantial C-terminal soluble (C^{Sol}) domain[19] (**Fig. S1**). Although pioneering "masochistic enzymology" studies[36] established the kinetic properties of yeast[20,21,37] and mammalian[38,39] PE methyltransferases, the functional significance of the duplicated catalytic domains, their potential communication during catalysis, and the role of the C^{Sol} domain remain unknown.

Here, we report four cryo-electron microscopy structures of fungal Cho2, including three structures of the transmembrane region at 3.20–2.56 Å resolution and a 3.26 Å structure of the isolated C^{Sol} domain. These structures reveal an elongated homodimer in which each protomer contains two homologous catalytic domains with distinct substrate-recognition mechanisms. Unexpectedly, biochemical and structural analyses suggest that the two active sites are tightly coupled through a communication helix, while an inhibitory nanobody reveals that the C^{Sol} domain positively regulates catalysis by facilitating cofactor binding. Together, our findings uncover multiple layers of regulation within the first and rate-limiting step of the PE methylation pathway and provide a structural framework for understanding phospholipid homeostasis in eukaryotes.

RESULTS

Biological and biochemical characterization of a fungal PE methyltransferase

To obtain a biochemically stable PE methyltransferase suitable for structural studies, we selected Cho2 from the thermophilic fungus *Chaetomium thermophilum* (*Ct*Cho2), which shares 30.3% sequence identity and 44.9% similarity with its *Saccharomyces cerevisiae* homolog (*Sc*Cho2) (**Fig. S1a**). To verify its biological function, we deleted *CHO2* in *Schizosaccharomyces pombe*, resulting in the previously reported[16] choline-auxotrophic phenotype. Episomal expression of *Ct*Cho2 fully rescued this growth defect, confirming that *Ct*Cho2 functions as a phosphatidylethanolamine *N*-methyltransferase *in vivo* (**Fig. 1a**).

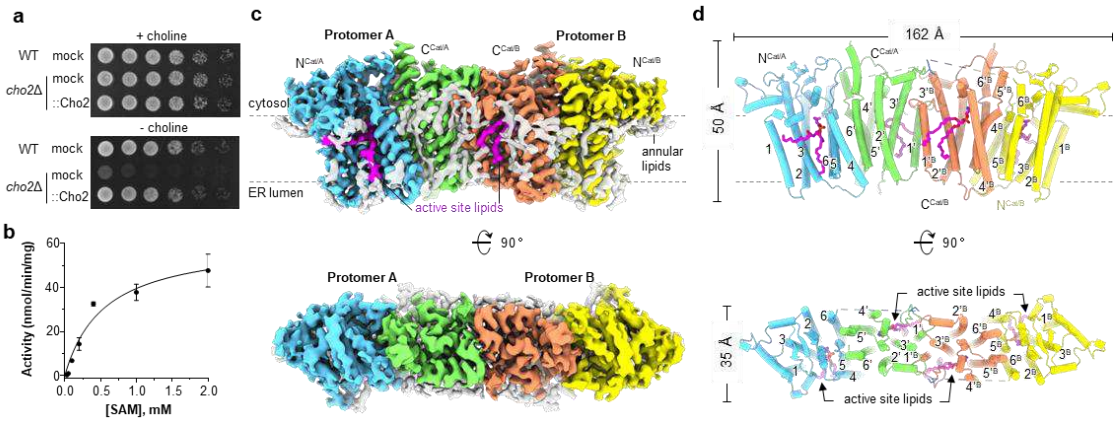


Fig. 1 | Structure and functional characterization of *Ct*Cho2. a Functional complementation of the *S. pombe cho2*Δ strain by heterogeneous expression of *Ct*Cho2. WT, wildtype *S. pombe*. **b** Michaelis-Menten analysis of *Ct*Cho2 for SAM. **c, d** Cryo-EM density map (**c**) and atomic model (**d**) of *Ct*Cho2 viewed from the membrane plane (top) or cytosol (bottom). Transmembrane helices (TMHs) are numbered as 1-6 for N^{Cat} and as 1'-6' for C^{Cat}. TMHs from protomer B are denoted with the superscript 'B'. Membrane boundaries are indicated by dash lines.

Purified *Ct*Cho2 (**Fig. S2a, S2b**) carrying a C-terminal thermostable GFP (TGP) tag[40] displayed the same strict substrate specificity reported for *Sc*Cho2[19], catalyzing methylation of PE but not phosphatidyl-N-monomethylethanolamine (PMME) (**Fig.**

S2c), thereby confirming its identity as a Cho2-type methyltransferase. In mixed micelles, *Ct*Cho2 followed Michaelis-Menten kinetics with SAM, reporting a K_m of 0.55 mM and a *V*max of 61.2 nmol min^{-1} mg^{-1} (**Fig. 1b**).

Structural determination

To elucidate the molecular basis of PE methylation, we determined three cryo-electron microscopy (cryo-EM) structures of *Ct*Cho2 representing distinct ligand-bound states. *Ct*Cho2 purified in glyco-diosgenin (GDN) yielded a 2.56-Å reconstruction (hereafter $Cho2^{PE/PC}$), whereas purification in the presence of SAH and PE or SAM and PMME produced the $Cho2^{PE}$ and $Cho2^{PMME}$ structures at 2.81-Å and 2.95-Å resolution, respectively (**Fig. 1c, 1d, Figs. S3, S5–S7; Table S1**). The cryo-EM maps revealed a C2-symmetric homodimer and enabled modeling of 517 residues (94.4% completeness) per protomer, encompassing all twelve transmembrane helices (TMHs). In contrast, density for the flexible N terminus, the TMH6-TMH7 linker, and the C-terminal soluble (C^{Sol}) domain was absent, suggesting that the C^{Sol} domain dissociates from the transmembrane region under the cryo-EM conditions.

Based on the cryo-EM densities together with the purification conditions (see Methods), PE and PMME were modeled into the catalytic pockets of $Cho2^{PE}$ and $Cho2^{PMME}$, respectively. In the absence of exogenous lipids, $Cho2^{PE/PC}$ instead contained endogenous phospholipids, with PC bound at the N-terminal catalytic site (N^{Cat}) and PE at the C-terminal catalytic site (C^{Cat}). In addition, multiple phospholipids and sterols were resolved around the transmembrane region, indicating extensive interactions with annular membrane lipids (**Fig. 1c, 1d**).

An elongated homodimer

Unless otherwise indicated, structural descriptions refer to $Cho2^{PE/PC}$. *Ct*Cho2 forms an elongated canoe-shaped homodimer measuring approximately 162 × 35 × 50 Å, with the C-terminal regions meeting at the center of the assembly and the N-terminal regions extending toward opposite ends (**Fig. 1c, 1d**). Each protomer comprises two

homologous catalytic domains, each containing six transmembrane helices (designated TMH1–6 and TMH1'–6', respectively) (**Fig. 1d, Fig. S4a, S4b**). The two protomers associate in a tail-to-tail arrangement mediated primarily by TMH1' and TMH3' together with their symmetry-related counterparts, burying approximately 2,140 $Å^2$ of surface area (**Fig. 2a**).

The dimer interface is stabilized by two salt bridges and two hydrogen bonds in the juxtamembrane region, together with extensive hydrophobic packing within the membrane. To assess the functional importance of dimerization, we introduced mutations designed to disrupt the interface. Whereas T386Y had little effect, S390Y, I394Y, and E456L reduced methyltransferase activity by approximately 20%, 40%, and 55%, respectively (**Fig. 2b**). Notably, these mutations did not exhibit degradation defects on SDS-PAGE (**Fig. S2c**), indicating that the reduced activity is unlikely to result from protein misfolding. These results suggest Cho2 requires dimerization for optimal activity.

Architecture of the individual catalytic domains

Consistent with their sequence similarity (20.2% identity and 37.7% similarity; **Fig. S1b**), the N^{Cat} and C^{Cat} domains adopt highly similar folds (Cα RMSD of 2.22 Å) and are related by an approximately 160° rotation within the membrane plane (**Fig. 1d, Fig. S4c, S4d**). In N^{Cat}, TMH2–6 form a tightly packed helical bundle, whereas TMH1 lies at the periphery of the domain (**Fig. 2c**). Despite its peripheral position, TMH1 is firmly anchored by the preceding membrane-buried α-helix (α1) and by an electrostatic interaction between its positively charged helix dipole and Glu174 on the amphipathic helix α3. TMH2–6 pack tightly together at the luminal leaflet but splay apart toward the cytosol, forming a three-sided phospholipid-binding cavity flanked by TMH2–3 and TMH4–5, with TMH6 forming its back wall (**Fig. 2c**). Above the cavity, an unusually long (40 residues) luminal loop connecting TMH4 and TMH5 caps the binding pocket. This connector is stabilized by the amphipathic helix α4, which anchors it to the membrane, and by β-strand pairing with two N-terminal β-strands (**Fig. 2c**).

Overall, the C^{Cat} domain adopts the same architecture as N^{Cat} with two notable differences. First, it lacks the N-terminal β-sheet. Second, the TMH4'–TMH5' connector bends toward TMH6' rather than away from it (**Fig. 2d**).

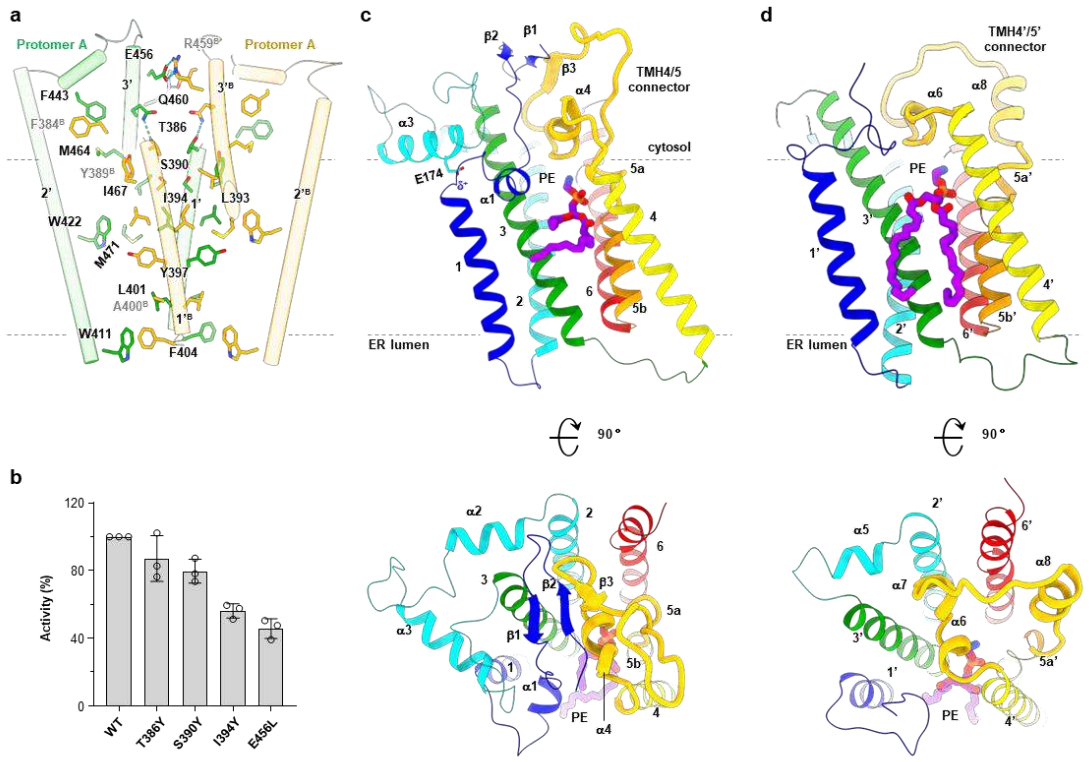


Fig. 2 | Overall architecture of *Ct*Cho2. a Dimer interface. Residues participating in intermolecular interactions are labeled. Dashed lines indicate hydrogen bonds or salt bridges within 3.4 Å. **b** Relative activities of dimer-interface mutants. Data represent mean ± s.d. from three independent experiments. **c, d** Structure of N^{Cat} (**c**) and C^{Cat} (**d**) domains viewed from the membrane plane (top) and the cytosol (bottom).

Molecular basis for substrate recognition at N^{Cat}

In the $Cho2^{PE}$ structure, the N^{Cat} active site contains a well-defined substrate-binding cavity that closely complements the ethanolamine head group and phosphoglycerol backbone of PE (**Fig. 3a**). Toward the membrane-facing end, the cavity gradually opens into the lipid bilayer, where one of the acyl chains is largely disordered (**Fig. 3b**). The ethanolamine head group is coordinated by an aromatic cage formed by Trp262, Tyr263, and Trp264, a recurring feature of methyltransferases[41]. The backbone carbonyl of

Trp262 further stabilizes the substrate through a hydrogen bond with the PE head group (**Fig. 3b**). Consistent with these interactions, mutation W262A completely abolished enzymatic activity, whereas Y263A reduced activity by approximately 95% (**Fig. 3c**). Notably, W262A completely abolished enzymatic activity despite leaving the corresponding C-terminal catalytic domain unaltered. The mechanistic basis of this unexpected effect will be discussed later.

The phosphoglycerol backbone is recognized through hydrogen bonds with Asn246, Lys250, and Ser290. Positioned at the narrow entrance of the substrate cavity, Asn246 appears to function as a steric gate controlling substrate access. Accordingly, subtle enlargement of its side chain (N246Q) reduced activity by ~90%, whereas constriction of the cavity entrance by G292L completely abolished catalysis (**Fig. 3c**). Together, these results indicate that PE recognition at the N^{Cat} site depends on both electrostatic complementarity and precise steric matching.

Molecular basis for substrate recognition at C^{Cat}

The C^{Cat} domain contains a substantially larger substrate-binding cavity that accommodates an entire ordered PE molecule (**Fig. 3d, 3e**). Measuring approximately 15 × 18 Å, the cavity is formed by TMH1'–5', with TMH1' and TMH4'–5' defining the sides and TMH2'–3' forming the back wall. Its interior is lined predominantly by hydrophobic and aromatic residues, with Trp481 and Tyr484 forming a hydrophobic floor at the base of the pocket (**Fig. 3d**). Unlike N^{Cat}, both PE acyl chains are fully enclosed within this hydrophobic environment. Near the glycerol ester bonds, however, the cavity narrows sharply through the juxtaposition of His473 and His509, which likely contribute both steric complementarity and electrostatic stabilization of the phosphate group (**Fig. 3e**).

As in N^{Cat}, the ethanolamine head group is coordinated by an aromatic cage. However, despite the presence of three consecutive aromatic residues in the TMH4'–TMH5' connector (**Fig. S1a**), only Trp525 and Tyr527 contribute directly, with Tyr465 from TMH3' completing the cage. Consistent with their structural roles, mutations W525A

and Y527A markedly reduced enzymatic activity (**Fig. 3c**). Together, these observations indicate that the two pseudo-symmetrical catalytic domains recognize PE through a conserved overall mechanism with distinct structural features.

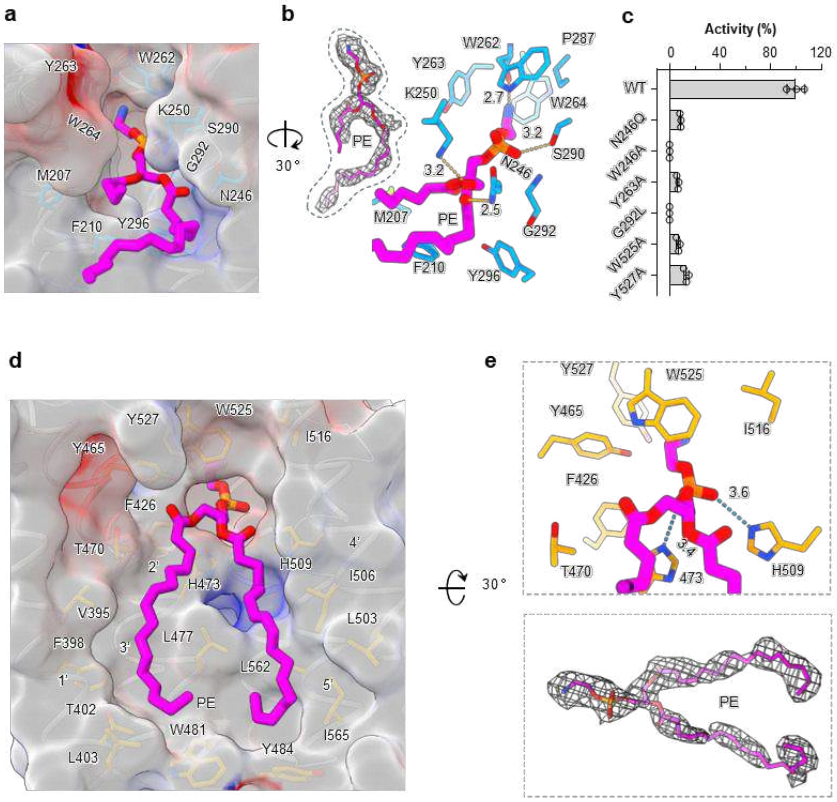


Fig. 3 | Molecular basis for phospholipid substrate recognition. a, b Surface (**a**) and stick (**b**) representation of the phosphatidylethanolamine (PE)-binding site in N^{Cat}. **c,** Relative activities of substrate-binding-site mutants. Data represent mean ± s.d. from three independent experiments. **d, e** Surface (**d**) and stick (**e**) representations of the PE-binding site in C^{Cat}. PE is shown in magenta, and the cryo-EM density is shown as a grey mesh (**b, e**).

Co-factor binding sites revealed by molecular modeling

Although SAM or SAH was included at high concentrations during sample preparation, no corresponding cryo-EM density attributable to these cofactors was observed in any of the reconstructed maps. To gain insight into cofactor recognition, we generated homology models of *Ct*Cho2 based on the structure of the homologous human PEMT bound to SAM (PDB ID 44UN), which we determined in a separate study. SAM was

subsequently docked into the two catalytic domains to predict potential cofactor-binding modes.

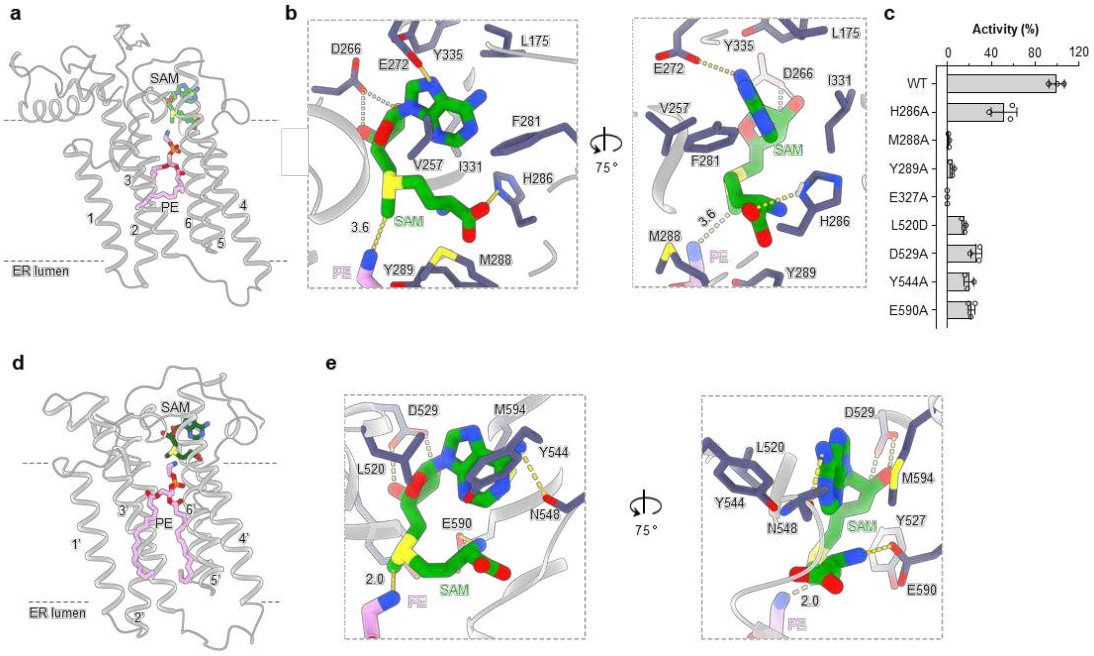


Fig. 4 | Structural model of cofactor binding. a, b Overview (**a**) and expanded view (**b**) of the proposed SAM-binding site in N^{Cat}. **c** Relative activities of mutants in the proposed SAM-binding site. Data represent mean ± s.d. from three independent experiments. **d, e** Overview (**d**) and expanded view (**e**) of the proposed SAM-binding site in C^{Cat}. Docked SAM is shown as green sticks. Dashed lines indicate predicted hydrogen bonds or the distance (Å) between the SAM methyl group and the reactive amine nitrogen of the experimentally determined PE.

In the N^{Cat} domain, the docked SAM molecule occupies a pocket formed primarily by the TMH4–TMH5 connector and TMH6 (**Fig. 4a, 4b**). The binding mode is supported by mutagenesis analyses, as substitution of residues surrounding the predicted cofactor-binding site, including E327A, H286A, M288A, and Y289A, substantially reduced or completely abolished catalytic activity (**Fig. 4c**). A highly similar cofactor-binding arrangement was observed in the C^{Cat} domain (**Fig. 4d, 4e**). Consistently, mutations targeting residues predicted to interact with SAM, including Leu520, Asp529, Tyr544, and Glu590, also strongly impaired enzymatic activity (**Fig. 4c**).

Notably, in both catalytic domains, the docked SAM molecules adopt conformations in which the transferable methyl group is positioned at an appropriate distance and angle relative to the PE amine group for an in-line transmethylation reaction (**Fig. 4b, 4e**). These models therefore suggest a plausible catalytic mechanism in which methyl transfer occurs through direct nucleophilic attack on the SAM methyl group.

Pre-organized active sites

The cryo-EM map of *Ct*Cho2 prepared in the presence of PMME contained densities consistent with PMME molecules bound in both catalytic domains (**Fig. S6d**). Relative to the PE-bound structure, $Cho2^{PMME}$ adopts a slightly more compact overall conformation, with an approximately 4-Å inward shift toward the dimer interface (**Fig. 5a**). In contrast, the substrate-binding pockets remain essentially unchanged, with nearly identical side-chain conformations throughout the catalytic cavities (**Figs. 5b, 5c**). The only notable local difference is a rotation of Trp262 within the N^{Cat} aromatic cage (**Fig. 5b**), likely to accommodate the additional methyl group of PMME. The near-identical active-site architectures of the PE- and PMME-bound structures suggest that the catalytic pockets are largely pre-organized before methyl transfer, requiring only minimal local rearrangement during catalysis.

Feedback inhibition by PC

As the first and rate-limiting enzyme in the PE methylation pathway, Cho2 represents a natural target for end-product feedback regulation. Consistent with this role, PC inhibited *Ct*Cho2 activity with an IC_{50} of 64 μM (**Fig. 5d**). Structural evidence for this inhibition was provided by the $Cho2^{PE/PC}$ structure, determined without exogenous lipids, in which the N^{Cat} active site contained a well-defined endogenous PC molecule. Its trimethylated head group produced a characteristic spherical density distinct from the sharper density of the PE molecule bound at the C^{Cat} active site (**Fig. 3e, 5e**). Together, these findings support a simple competitive mechanism in which PC directly inhibits Cho2 by occupying the PE-binding site, thereby coupling enzyme activity to the cellular PE/PC ratio.

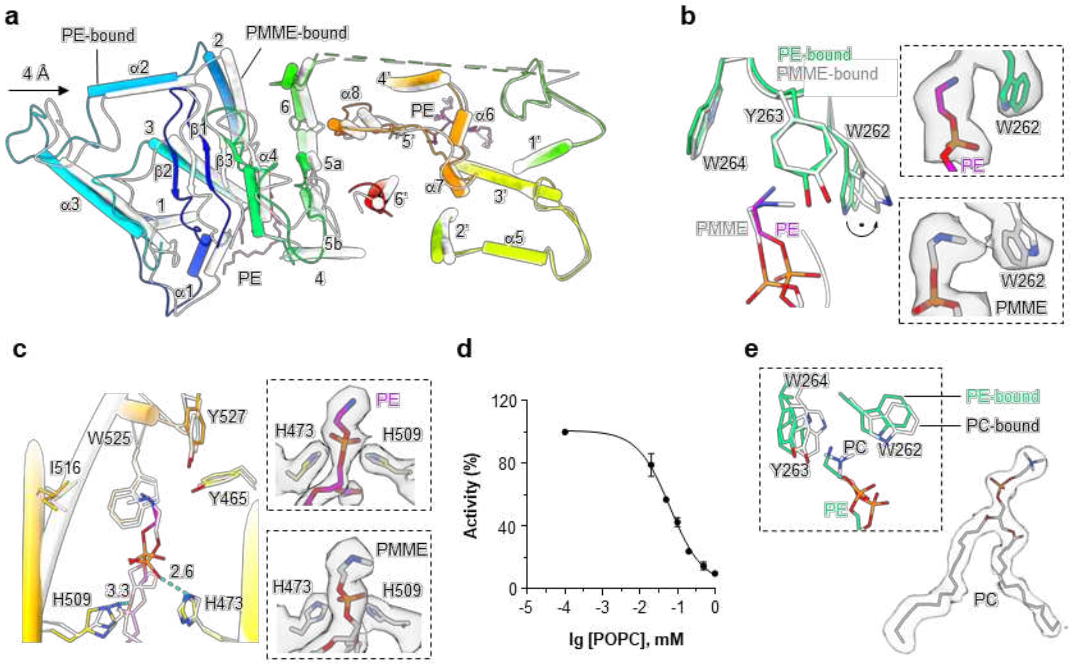


Fig. 5 | Structural comparison of different ligand-bound states. a, Superposition of the PE-bound (rainbow) and PMME-bound (grey) *Ct*Cho2 structures. **b, c** Close-up views of the N^{Cat} (**b**) and C^{Cat} (**c**) active sites. Representative cryo-EM densities are shown as semi-transparent surfaces. **d** Inhibition of *Ct*Cho2 by POPC. Data represent mean ± s.d. from three independent experiments. **e** Comparison of the PE-bound (green) and PC-bound (grey) N^{Cat} active sites. The cryo-EM density corresponding to bound PC is shown as a semi-transparent surface.

The C-terminal soluble domain promotes cofactor binding

The simultaneous absence of resolved SAM/SAH density and the C-terminal soluble domain (C^{Sol}) in all cryo-EM structures prompted us to investigate whether the C^{Sol} domain contributes to cofactor recognition or stabilization. Deletion of the C^{Sol} domain caused substantial, but not complete, loss of *Ct*Cho2 activity (**Fig. 6a**), indicating that the transmembrane catalytic core alone remains functional. However, ΔC^{Sol} displayed lower SAM affinity, reporting an apparent K_m (2.7 mM) (**Fig. 6b**) that is 5-fold of the full-length enzyme (**Fig. 1b**). These results indicate that the C^{Sol} domain likely promotes efficient cofactor binding during catalysis.

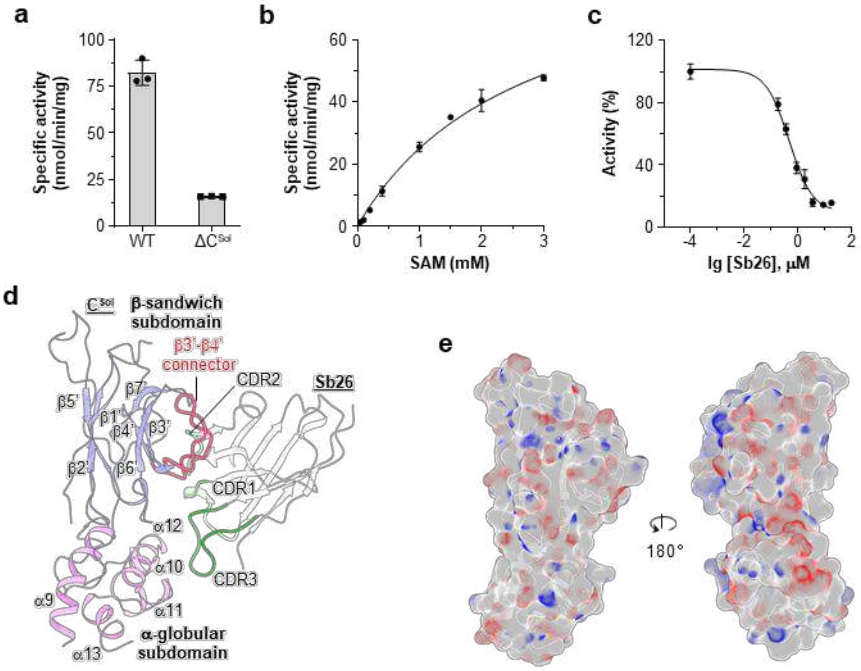


Fig. 6 | Functional and structural characterization of the C^{Sol} domain. a Effect of C-terminal truncation on *Ct*Cho2 activity. **b** Michaelis-Menten analysis of the C^{Sol} truncation mutant. **c** Inhibition of *Ct*Cho2 by the C^{Sol}-targeting nanobody Sb26. **d** Structure of the C^{Sol}-Sb26 complex. The β-sandwich and α-helical subdomains of C^{Sol} are colored blue and pink, respectively. The β3–β4 connector is highlighted in red. Sb26 is shown in white, with the complementarity-determining regions (CDRs) indicated. **e,** Electrostatic surface representation of C^{Sol}. Red and blue denote negatively and positively charged regions, respectively.

An inhibitor nanobody acts on the regulatory C^{Sol} domain

As an attempt to stabilize the interaction between the C^{Sol} and transmembrane domains for structural analysis, we screened an inhibitory synthetic nanobody[42], designated Sb26 (**Fig. 6c**). However, cryo-EM analysis of the *Ct*Cho2-Sb26 complex failed to resolve either the C^{Sol} domain or Sb26, suggesting that Sb26 inhibits *Ct*Cho2 by binding to and sequestering the highly mobile C^{Sol} domain rather than stabilizing its association with the transmembrane region.

To determine the architecture of C^{Sol}, we solved the cryo-EM structure of the C^{Sol}-Sb26

complex at 3.26-Å resolution using the Legobody strategy[43]. C^{Sol} comprises two tightly associated subdomains: a β-sandwich formed by opposing three- and four-stranded β-sheets, and a compact five-helix α-globular domain (**Fig. 6d**). The β-sandwich domain contains an extended β3–β4 loop that folds back onto the domain, reminiscent of the ligand- and protein-binding loops found in jelly-roll[44,45] and nanobody folds[42] (**Fig. 6d**). Notably, the C^{Sol} surface lacks extensive hydrophobic patches (**Fig. 6e**), arguing against stable hydrophobic association with the transmembrane domain. Instead, C^{Sol} is likely to interact transiently with the cytosolic face of the membrane region through polar contacts, consistent with its proposed role in promoting SAM binding.

Coupling between the two catalytic domains

The unexpected complete loss of activity caused by several single-point mutations confined to a single catalytic domain (**Figs. 3c, 4c**) indicates that the N^{Cat} and C^{Cat} active sites are functionally coupled rather than operating independently. Consistent with this conclusion, isolated N^{Cat} and C^{Cat} domains (**Fig. S8a**) exhibited little or no detectable activity (**Fig. 7a**), demonstrating that the dual-domain architecture is essential for catalysis.

To investigate the structural basis of this coupling, we compared the experimentally determined *Ct*Cho2 structures, which likely represent resting conformations, with homology models based on the aforementioned SAM-bound human PEMT structure (PDB entry 44UN), which approximate an active state. The comparison revealed coordinated rearrangements of the TMH4–TMH5 and TMH4'–TMH5' connectors. In the proposed active conformation, movement of the N^{Cat} connector organizes the N^{Cat} SAM-binding pocket while simultaneously displacing helix α8, hereafter referred to as the communication helix. Because α8 forms part of the C^{Cat} connector, this movement concomitantly reorganizes the C^{Cat} SAM-binding pocket (**Fig. 7b–7d; Movie 1**).

Notably, Tyr544 serves a dual role during this transition. In the resting conformation,

it occludes the N^{Cat} SAM-binding site, whereas in the modeled active state it rotates by ~180° to become a component of the C^{Cat} SAM-binding pocket. (**Fig. 4e, 7e; Movie 1**). This dual role provides a structural explanation for the tight coupling between the two catalytic domains.

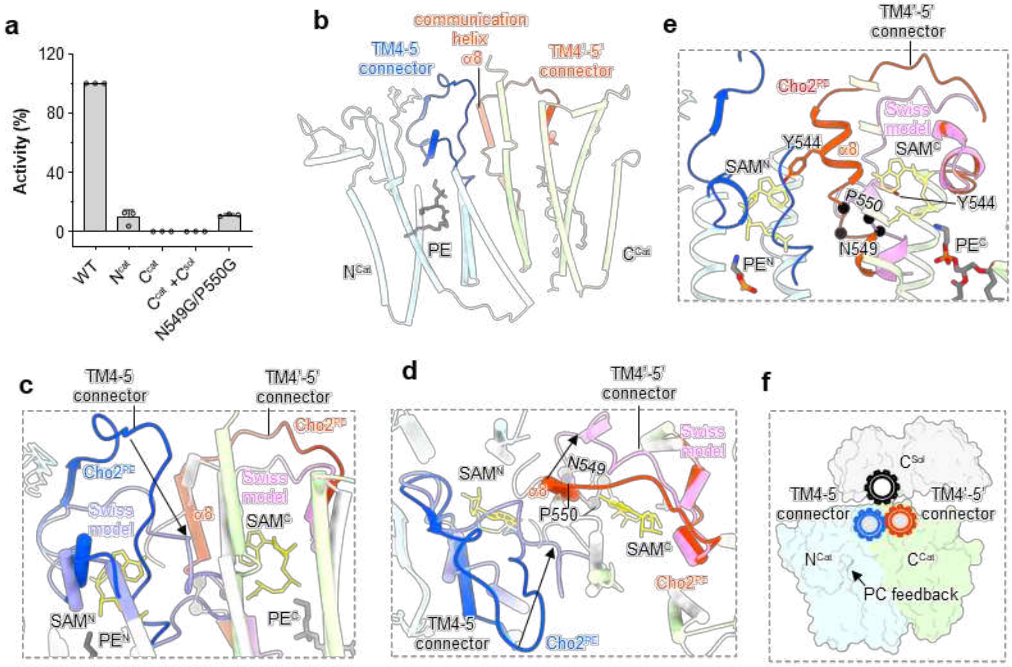


Fig. 7 | Coupling between the two catalytic domains. a Relative activities of truncation and mutant constructs. Data represent mean ± s.d. from three independent experiments. **b–d** Overall (**b**), side (**c**), and cytosolic (**d**) views of the TMH4–TMH5 and TMH4'–TMH5' connector regions. Experimentally determined structures are colored as in **Fig. 2**, whereas the predicted active-state model is shown in grey, with the N^{Cat} and C^{Cat} connector regions highlighted in light blue and pink, respectively. **e** Close-up view of the communication helix (α8, red) involved in coupling the two active sites. The experimentally determined structure is colored as in **b**, whereas the predicted active-state connector is shown in pink. Docked SAM molecules are shown as yellow sticks. **f** Proposed model for *Ct*Cho2 regulation. The C^{Sol} domain promotes SAM binding, the communication helix couples the two catalytic domains, and PC inhibits *Ct*Cho2 through feedback binding to the N^{Cat} active site.

To test whether the communication helix actively transmits conformational changes, we increased its local flexibility by introducing the double mutation N549G/P550G. The resulting loss of activity (**Fig. 7a**) supports a model in which structural rigidity of the communication helix is required for efficient communication between the two active sites.

Together, our structural and biochemical data support a working model in which the C^{Sol} domain binds the TMH4–TMH5 and TMH4'–TMH5' connectors, simultaneously organizing both SAM-binding sites (**Fig. 7f**). Following catalysis, C^{Sol} dissociates from the transmembrane domain, resetting the enzyme to its resting state, in which Tyr544 switches from a component of the C^{Cat} SAM-binding pocket to an occluder of the N^{Cat} pocket (**Fig. 7e; Movie 1**). Despite extensive efforts, we were unable to capture an active, cofactor-bound state that would directly validate this proposed conformational transition and clarify the roles of C^{Sol} and Tyr544, which will therefore require future structural studies.

DISCUSSION

Phospholipid homeostasis influence myriad fundamental cellular processes, including membrane organization, lipid metabolism, stress responses, autophagy, and epigenetic regulation[1]. The PE methylation pathway contributes to this homeostasis by controlling the cellular PE/PC ratio. Because PC biosynthesis through PE methylation consumes substantial amounts of SAM, Cho2 also links phospholipid metabolism to one-carbon metabolism, thereby influencing diverse methylation-dependent pathways such as histone methylation[6] and mitochondrial function[30]. Here, we present the structural characterization of Cho2, the enzyme catalyzing the first and rate-limiting step of the PE methylation pathway[20], revealing the molecular basis of substrate recognition and multiple layers of enzymatic regulation.

An intriguing evolutionary question is why fungi require two homologous enzymes to catalyze the three sequential methylation reactions converting PE to PC, whereas mammals employ a single enzyme for all three steps[36]. This complexity is further amplified by the unusual architecture of Cho2 itself. Unlike the compact mammalian PEMT, Cho2 contains two internally pseudo-symmetrical catalytic domains, a regulatory C-terminal soluble (C^{Sol}) domain, and forms a homodimer, resulting in four active sites per dimer. Rather than acting as independent enzymes, our data indicate that the duplicated domains have evolved into a tightly coupled catalytic unit. Such architectural complexity likely reflects the need for extensive regulation of the first and committed step of the PE methylation pathway, analogous to how the oligomeric architecture of hemoglobin enables regulatory properties absent from the monomeric myoglobin.

Consistent with this view, our study identifies multiple regulatory mechanisms governing Cho2 activity. First, *Ct*Cho2 is subject to feedback inhibition by the pathway end product PC, providing a direct mechanism by which enzyme activity can respond to membrane phospholipid composition. Second, the two catalytic domains are functionally coupled, with perturbation of either active site abolishing overall

catalytic activity. Structural modeling suggests that this coupling is mediated by coordinated rearrangements of the connector regions and the communication helix linking the two active sites. Third, the C^{Sol} domain positively regulates catalysis by facilitating cofactor binding, and this regulatory function can be disrupted by an inhibitory nanobody. Together, these mechanisms reveal that Cho2 integrates membrane lipid composition, inter-domain communication, and cofactor binding into a highly coordinated regulatory network.

The regulatory role of the C^{Sol} domain raises the possibility that Cho2 activity is further modulated by endogenous protein partners. The observation that nanobody binding to the isolated C^{Sol} domain inhibits catalysis suggests that cellular factors may similarly regulate Cho2 through this region. Future studies combining protein interaction screening with biochemical validation will be important for identifying such regulatory partners.

Our structural observations also raise the possibility that Cho2 is regulated not only by phospholipid composition but also by the physical properties of the membrane. Mammalian PEMT, which is homologous to N^{Cat} and C^{Cat}, displays a marked increase in activity when detergent micelles transition to a bicelle-like environment[38], indicating that membrane architecture may directly modulate catalysis. Given its unusually large membrane footprint (~162 Å), Cho2 may be particularly sensitive to membrane curvature or lipid packing. In support of this idea, the PMME- and PC-bound structures adopt a slightly more compact conformation than the PE-bound state, potentially making them more compatible with flatter, PC-rich membranes. Although this possibility remains highly speculative, our observations raise the intriguing possibility that membrane mechanics may provide an additional layer of regulation for Cho2 activity. Future biochemical and biophysical studies using membranes with defined curvature, lipid composition, and packing properties will be required to test this hypothesis directly.

An intriguing finding is that the N^{Cat} active site accommodates PC with little structural rearrangement, despite the strict substrate specificity of Cho2, in which PMME and phosphatidyl-*N*-dimethylethanolamine are not substrates. Although the mechanism underlying PE specificity remains unknown, this observation suggests that phospholipid binding and productive catalysis are governed by distinct determinants, with methyl transfer requiring a more stringent catalytic geometry than substrate recognition alone. Such a mechanism may allow Cho2 to bind PC for feedback inhibition while preventing promiscuous methylation of mono- or di-methylated PE.

Finally, despite extensive efforts, we were unable to obtain an experimental structure of Cho2 containing bound SAM or SAH. Our proposed cofactor-binding mode and the role of the communication helix are therefore based on structural modeling together with extensive mutagenesis and biochemical analyses, rather than on a directly resolved cofactor-bound state. The apparent absence of tightly bound SAH is notable because SAH commonly acts as a potent product inhibitor of methyltransferases. Indeed, in our parallel study of human PEMT, endogenous SAH remained tightly associated with the recombinant enzyme even after extensive purification. Because Opi3 is structurally homologous to mammalian PEMT, it is possible that Opi3 is similarly regulated by SAH, whereas Cho2 may employ alternative regulatory mechanisms involving inter-domain communication and the C^{Sol} domain. Such divergence may enable fungal cells to independently regulate distinct steps of the PE methylation pathway in response to different metabolic signals. Future structures of Cho2 in defined catalytic states, particularly cofactor-bound states, will be important for determining whether the proposed conformational transition and the roles of C^{Sol} and Tyr544 occur as modeled.

REFERENCES

1. van der Veen, J.N. et al. The critical role of phosphatidylcholine and phosphatidylethanolamine metabolism in health and disease. *Biochim Biophys Acta Biomembr* **1859**, 1558-1572 (2017).
2. Tamura, Y., Kawano, S. & Endo, T. Lipid homeostasis in mitochondria. *Biol Chem* **401**, 821-833 (2020).
3. Gao, X. et al. Lack of phosphatidylethanolamine N-methyltransferase alters hepatic phospholipid composition and induces endoplasmic reticulum stress. *Biochim Biophys Acta* **1852**, 2689-99 (2015).
4. Polyansky, A. et al. Phospholipid imbalance impairs autophagosome completion. *Embo j* **41**, e110771 (2022).
5. Sakakibara, K. et al. Phospholipid methylation controls Atg32-mediated mitophagy and Atg8 recycling. *Embo j* **34**, 2703-19 (2015).
6. Ye, C., Sutter, B.M., Wang, Y., Kuang, Z. & Tu, B.P. A Metabolic Function for Phospholipid and Histone Methylation. *Mol Cell* **66**, 180-193.e8 (2017).
7. Fang, W., Zhu, Y., Yang, S., Tong, X. & Ye, C. Reciprocal regulation of phosphatidylcholine synthesis and H3K36 methylation programs metabolic adaptation. *Cell Rep* **39**, 110672 (2022).
8. Song, J. et al. Polymorphism of the PEMT gene and susceptibility to nonalcoholic fatty liver disease (NAFLD). *Faseb j* **19**, 1266-71 (2005).
9. Sun, C. et al. The Role of Phosphatidylethanolamine N-Methyltransferase (PEMT) and Its Waist-Hip-Ratio-Associated Locus rs4646404 in Obesity-Related Metabolic Traits and Liver Disease. *Int J Mol Sci* **24**(2023).
10. Sharma, N.K., Langberg, K.A., Mondal, A.K. & Das, S.K. Phospholipid biosynthesis genes and susceptibility to obesity: analysis of expression and polymorphisms. *PLoS One* **8**, e65303 (2013).
11. Tajuddin, S.M. et al. LINE-1 methylation in leukocyte DNA, interaction with phosphatidylethanolamine N-methyltransferase variants and bladder cancer risk. *Br J Cancer* **110**, 2123-30 (2014).
12. Xu, X. et al. Choline metabolism and risk of breast cancer in a population-based study. *Faseb j* **22**, 2045-52 (2008).
13. Noga, A.A., Zhao, Y. & Vance, D.E. An unexpected requirement for phosphatidylethanolamine N-methyltransferase in the secretion of very low density lipoproteins. *J Biol Chem* **277**, 42358-65 (2002).
14. van der Veen, J.N., Lingrell, S., da Silva, R.P., Jacobs, R.L. & Vance, D.E. The concentration of phosphatidylethanolamine in mitochondria can modulate ATP production and glucose metabolism in mice. *Diabetes* **63**, 2620-30 (2014).
15. Gao, X. et al. Decreased lipogenesis in white adipose tissue contributes to the resistance to high fat diet-induced obesity in phosphatidylethanolamine N-methyltransferase-deficient mice. *Biochim Biophys Acta* **1851**, 152-62 (2015).

16. Kanipes, M.I. & Henry, S.A. The phospholipid methyltransferases in yeast. *Biochimica et Biophysica Acta (BBA) - Lipids and Lipid Metabolism* **1348**, 134-141 (1997).
17. Carman, G.M. & Han, G.S. Regulation of phospholipid synthesis in yeast. *J Lipid Res* **50 Suppl**, S69-73 (2009).
18. Summers, E.F., Letts, V.A., McGraw, P. & Henry, S.A. Saccharomyces cerevisiae cho2 mutants are deficient in phospholipid methylation and cross-pathway regulation of inositol synthesis. *Genetics* **120**, 909-22 (1988).
19. Kodaki, T. & Yamashita, S. Yeast phosphatidylethanolamine methylation pathway. Cloning and characterization of two distinct methyltransferase genes. *J Biol Chem* **262**, 15428-35 (1987).
20. Gaynor, P.M. & Carman, G.M. Phosphatidylethanolamine methyltransferase and phospholipid methyltransferase activities from Saccharomyces cerevisiae. Enzymological and kinetic properties. *Biochim Biophys Acta* **1045**, 156-63 (1990).
21. Kodaki, T. & Yamashita, S. Characterization of the methyltransferases in the yeast phosphatidylethanolamine methylation pathway by selective gene disruption. *Eur J Biochem* **185**, 243-51 (1989).
22. Boumann, H.A. et al. Depletion of phosphatidylcholine in yeast induces shortening and increased saturation of the lipid acyl chains: evidence for regulation of intrinsic membrane curvature in a eukaryote. *Mol Biol Cell* **17**, 1006-17 (2006).
23. Shyu, P., Jr. et al. Membrane phospholipid alteration causes chronic ER stress through early degradation of homeostatic ER-resident proteins. *Sci Rep* **9**, 8637 (2019).
24. Thibault, G. et al. The membrane stress response buffers lethal effects of lipid disequilibrium by reprogramming the protein homeostasis network. *Mol Cell* **48**, 16-27 (2012).
25. Ho, N. et al. Stress sensor Ire1 deploys a divergent transcriptional program in response to lipid bilayer stress. *J Cell Biol* **219**(2020).
26. Wilson-Zbinden, C. et al. Autophagy competes for a common phosphatidylethanolamine pool with major cellular PE-consuming pathways in Saccharomyces cerevisiae. *Genetics* **199**, 475-85 (2015).
27. Fei, W. et al. A role for phosphatidic acid in the formation of "supersized" lipid droplets. *PLoS Genet* **7**, e1002201 (2011).
28. Malanovic, N. et al. S-adenosyl-L-homocysteine hydrolase, key enzyme of methylation metabolism, regulates phosphatidylcholine synthesis and triacylglycerol homeostasis in yeast: implications for homocysteine as a risk factor of atherosclerosis. *J Biol Chem* **283**, 23989-99 (2008).
29. Perez, M.F. & Sarkies, P. Histone methyltransferase activity affects metabolism in human cells independently of transcriptional regulation. *PLoS Biol* **21**, e3002354 (2023).

30. Ayer, A. et al. Genetic screening reveals phospholipid metabolism as a key regulator of the biosynthesis of the redox-active lipid coenzyme Q. *Redox Biol* **46**, 102127 (2021).
31. Sadhu, M.J., Moresco, J.J., Zimmer, A.D., Yates, J.R., 3rd & Rine, J. Multiple inputs control sulfur-containing amino acid synthesis in Saccharomyces cerevisiae. *Mol Biol Cell* **25**, 1653-65 (2014).
32. Albuquerque, P. et al. Quorum sensing-mediated, cell density-dependent regulation of growth and virulence in Cryptococcus neoformans. *mBio* **5**, e00986-13 (2013).
33. Kundu, D., Hameed, S., Fatima, Z. & Pasrija, R. Phospholipid biosynthesis disruption renders the yeast cells sensitive to antifungals. *Folia Microbiol (Praha)* **65**, 121-131 (2020).
34. Pawlik, G., Renne, M.F., Kol, M.A. & de Kroon, A. The topology of the ER-resident phospholipid methyltransferase Opi3 of Saccharomyces cerevisiae is consistent with in trans catalysis. *J Biol Chem* **295**, 2473-2482 (2020).
35. Shields, D.J., Lehner, R., Agellon, L.B. & Vance, D.E. Membrane topography of human phosphatidylethanolamine N-methyltransferase. *J Biol Chem* **278**, 2956-62 (2003).
36. Vance, D.E. From masochistic enzymology to mechanistic physiology and disease. *J Biol Chem* **292**, 17169-17177 (2017).
37. Boumann, H.A., Chin, P.T., Heck, A.J., De Kruijff, B. & De Kroon, A.I. The yeast phospholipid N-methyltransferases catalyzing the synthesis of phosphatidylcholine preferentially convert di-C16:1 substrates both in vivo and in vitro. *J Biol Chem* **279**, 40314-9 (2004).
38. Ridgway, N.D. & Vance, D.E. Kinetic mechanism of phosphatidylethanolamine N-methyltransferase. *J Biol Chem* **263**, 16864-71 (1988).
39. Ridgway, N.D. & Vance, D.E. Specificity of rat hepatic phosphatidylethanolamine N-methyltransferase for molecular species of diacyl phosphatidylethanolamine. *J Biol Chem* **263**, 16856-63 (1988).
40. Cai, H. et al. An improved fluorescent tag and its nanobodies for membrane protein expression, stability assay, and purification. *Commun Biol* **3**, 753 (2020).
41. Vann, K.R., Vishweshwaraiah, Y.L., Dokholyan, N.V. & Kutateladze, T.G. Searching for methyllysine-binding aromatic cages. *Biochem J* **478**, 3613-3619 (2021).
42. Zimmermann, I. et al. Synthetic single domain antibodies for the conformational trapping of membrane proteins. *eLife* **7**, e34317 (2018).
43. Wu, X. & Rapoport, T.A. Cryo-EM structure determination of small proteins by nanobody-binding scaffolds (Legobodies). *Proceedings of the National Academy of Sciences* **118**, e2115001118 (2021).
44. Hashimoto, H. Recent structural studies of carbohydrate-binding modules. *Cell Mol Life Sci* **63**, 2954-67 (2006).

45. Yan, R. et al. Human SEIPIN Binds Anionic Phospholipids. *Dev Cell* **47**, 248-256.e4 (2018).
46. Huang, S. et al. Identification of Methylosome Components as Negative Regulators of Plant Immunity Using Chemical Genetics. *Mol Plant* **9**, 1620-1633 (2016).
47. Matsuyama, A. et al. pDUAL, a multipurpose, multicopy vector capable of chromosomal integration in fission yeast. *Yeast* **21**, 1289-305 (2004).
48. Li, T. et al. Uncovering a conserved vulnerability site in SARS-CoV-2 by a human antibody. *EMBO Mol Med* **13**, e14544 (2021).
49. Cai, H., Yao, H., Li, T., Tang, Y. & Li, D. High-level heterologous expression of the human transmembrane sterol Δ8,Δ7-isomerase in Pichia pastoris. *Protein Expr Purif* **164**, 105463 (2019).
50. Li, T. et al. A synthetic nanobody targeting RBD protects hamsters from SARS-CoV-2 infection. *Nature Communications* **12**, 4635 (2021).
51. Punjani, A., Rubinstein, J.L., Fleet, D.J. & Brubaker, M.A. cryoSPARC: algorithms for rapid unsupervised cryo-EM structure determination. *Nature Methods* **14**, 290-296 (2017).
52. Bepler, T. et al. Positive-unlabeled convolutional neural networks for particle picking in cryo-electron micrographs. *Nat Methods* **16**, 1153-1160 (2019).
53. Casañal, A., Lohkamp, B. & Emsley, P. Current developments in Coot for macromolecular model building of Electron Cryo-microscopy and Crystallographic Data. *Protein Sci* **29**, 1069-1078 (2020).
54. Liebschner, D. et al. Macromolecular structure determination using X-rays, neutrons and electrons: recent developments in Phenix. *Acta Crystallogr D Struct Biol* **75**, 861-877 (2019).
55. Goodsell, D.S., Sanner, M.F., Olson, A.J. & Forli, S. The AutoDock suite at 30. *Protein Sci* **30**, 31-43 (2021).
56. Meng, E.C. et al. UCSF ChimeraX: Tools for structure building and analysis. *Protein Sci* **32**, e4792 (2023).

METHODS

Molecular cloning

The codon-optimized gene encoding Cho2 from *Chaetomium thermophilum* (GenBank: GL988041) was synthesized by Azenta (Suzhou, China) and sub-cloned into the yeast expression vector pYTSG between the *BamH*I/*Kpn*I restriction sites by T4 ligation. A DNA fragment encoding twin-Strep was added to the extreme C-terminus by insertion PCR (polymerase chain reaction). The resulting constructed is designated pYTSG-*Ct*Cho2 and encoding a protein with the following order (from N- to C-terminus): *Ct*Cho2, 3C protease site, TGP, and a Twin-Strep tag. For sybody selection, an Avi-tag (GLNDIFEAQKIEWHE) was inserted between *Ct*Cho2 and the 3C protease site of pYTSG-*Ct*Cho2. For rescue experiment, the DNA fragment encoding *Ct*Cho2-TGP was subcloned into pDB1614[46,47] using *BamH*I and *BssH*II using Gibson assembly.

All truncation constructs were made based on the pYTSG-*Ct*Cho2 backbone. Residues for the constructs are as follows: ΔC^{Sol}, residues 1-607; N^{Cat}, residues 1-336; C^{Cat}, residues 371-607; C^{Sol}, residues 672-944; and $C^{Cat} + C^{Sol}$, residues 371-959. Cho2 mutants were generated by site-directed mutagenesis. Truncation mutants were generated using deletion PCR. All constructs were verified by Sanger sequencing.

Pombe KO and rescue

The *CHO2* deletion strain in *S. pombe* LD259 (*h+ ura4-D18 leu1-32 his3-D1*) was generated by homologous recombination. The KanMX resistance cassette was PCR-amplified from a plasmid using primers KanMX_F (5'-GGCGCGCCAGATCTGTTTAG-3') and KanMX_R (5'-GGATGGCGGCGTTAGTATCG-3'). DNA fragments corresponding to the 5' and 3' homologous arms of *CHO2* were amplified from LD259 genomic DNA using primer pairs up_F (5′-AGTGTCTACCAAACTCGTGTTC-3′)/up_R (5'-CTAAACAGATCTGGCGCGCCATTTGAATATATGGGTATTTTATCAAAACT-3') and down_F (5'-

CGATACTAACGCCGCCATCCATATTCAACAATTTTATGATTTATTCATTCAAC AT-3')/down_R (5'-TTATAATCAATTTCATTTTGACACGATTTCC-3'), respectively. The three PCR products were assembled by overlap-extension PCR to generate the deletion cassette, which was transformed into LD259. Transformants were selected on G418-containing medium supplemented with choline. Correct integration was verified by PCR using primers ver_F (5'-GGGAAGCTCGATTTGTCTGC-3') and ver_KanMX_R (5'-GGTATTCTGGGCCTCCATGTCGC-3').

The complementation plasmid pDB1614-*Ct*Cho2 was transformed into the *cho2*Δ strain. Transformants were selected on Synthetic Dropout medium lacking uracil (SD-ura, 18 mg L^{-1} adenine, 8 mg L^{-1} of p-aminobenzoic acid, 76 mg L^{-1} myo-inositol, and 0.67 % (w/v) yeast nitrogen base (YNB), 76 mg L^{-1} of Ala, Arg, Asn, Asp, Cys, Glu, Gln, Gly, His, Ile, Lys, Met, Phe, Pro, Ser, Thr, Trp, Tyr, Val, and 380 mg L^{-1} of Leu) supplemented with 2% (w/v) glucose. Unless otherwise indicated, *S. pombe* cells were cultured at 30 °C. Overnight cultures grown in SD-ura medium supplemented with 1 mM choline were diluted into fresh medium to an initial OD_{600} of 0.2 and grown to an OD_{600} of approximately 0.6. Cells were harvested, washed three times with TE buffer (50 mM Tris-HCl, pH 8.0, 1 mM EDTA) to remove residual choline, resuspended to an OD_{600} of 1.0, and spotted as 5-µL aliquots of fivefold serial dilutions onto SD-ura agar plates with or without 5 mM choline.

Expression and purification – *Ct*Cho2

All yeast cells were grown at 30 °C in this study. The plasmid pYTSG-*Ct*Cho2 was transformed into *Saccharomyces cerevisiae* BCY123 (*pep4::HIS3 prb1::LEU2 bar1::HISG lys2::Gal1/10-Gal4 can1 ade2 trp1 his3 ura3 leu2-3,112 lys2*) using the lithium acetate heat-shock method. Transformants were selected on synthetic complete (SC) medium lacking uracil (SC-ura, 18 mg L^{-1} adenine, 8 mg L^{-1} of p-aminobenzoic acid, 76 mg L^{-1} myo-inositol, and 0.67 % (w/v) yeast nitrogen base (YNB), 76 mg L^{-1} of Ala, Arg, Asn, Asp, Cys, Glu, Gln, Gly, His, Ile, Lys, Met, Phe, Pro, Ser, Thr, Trp,

Tyr, Val, and 380 mg L^{-1} of Leu) supplemented with 2% (w/v) glucose. A single colony was inoculated into 3 mL SC-Ura medium and cultured overnight at 30 °C with shaking at 220 rpm. The culture was expanded into 300 mL in the same medium, and subsequently diluted into 900 mL SC-ura supplemented with 0.1 %(w/v) glucose to an initial OD_{600} of 0.12-0.15. Cells were grown to an OD_{600} of 0.55–0.60 (typically 8 h) before expression was induced by addition of galactose to a final concentration of 2% (w/v). After incubation for 20 h at 25 °C, cells were harvested by centrifugation at 4,000 × g for 15 min, and resuspended in **Buffer A** (150 mM NaCl, 10% (v/v) glycerol, 50 mM Tris-HCl pH 8.0) supplemented with 1 mM phenylmethylsulfonyl fluoride (PMSF), frozen in liquid nitrogen and disrupted using a freezer mill (SPEX 6875) followed by high-pressure homogenization (UH-06, Union, Shanghai, China) at 600–700 bar. Cell debris was removed by centrifugation at 3,000 × g for 15 min, and membranes were collected by centrifugation at 60,000 × g for 1.5 h. Membranes were resuspended in storage buffer (1 mM PMSF, 150 mM NaCl, 40% (v/v) glycerol, and 50 mM Tris-HCl pH 8.0), flash-frozen in liquid nitrogen and stored at -80 °C.

All purification procedures were performed on ice or at 4 °C. Membranes were diluted fourfold with **Buffer B** (150 mM NaCl, 50 mM Tris-HCl pH 8.0) supplemented with 0.2 mM tris(2-carboxyethyl)phosphine (TCEP) and 1 mM PMSF and solubilized with 1% (w/v) *n*-dodecyl-β-D-maltoside (DDM) DDM for 1.5 h. Insoluble material was removed by centrifugation at 48,000 × g for 1 h, and the supernatant was incubated with Strep-Tactin resin (Cat. SA053100, Smart-lifesciences, Changzhou, China) for affinity purification. Beads were washed with 5 column-volume (CV) wash Buffer A supplemented with 0.03 % DDM, 0.01 % GDN, 0.2 mM TCEP, and 1.5 CV with Buffer A supplemented with 0.1 % glyco-diosgenin (GDN), 0.2 mM TCEP. After a 10 min-incubation, the column was washed with 1.5 CV 0.1 % GDN, 0.2 mM TCEP in Buffer A and 3 CV 0.008 % GDN, 0.2 mM TCEP in Buffer A. *Ct*Cho2 was then eluted with 5 mM D-dethiobiotin and further purified using gel filtration on a Superose 6 Increase 10/300 GL column (Cat. 29-0915-96, Cytiva, Marlborough, MA, USA) equilibrated in 0.008 % GDN, 150 mM NaCl, 0.2 mM TCEP and 20 mM Tris 8.0. Peak fractions were

pooled and concentrated to 5.4 mg mL^{-1} for Cryo-EM. Protein was quantified using absorbance at 280 nm with the theoretical extinction coefficient of 265,815 M^{-1} cm^{-1}.

For preparation of the $Cho2^{PE}$ sample, purification followed the procedure described above except that 1-palmitoyl-2-oleoyl-sn-glycero-3-phosphoethanolamine (POPE, Cat. 850757P, Avanti, Alabaster, AL, USA) was included throughout detergent exchange and size-exclusion chromatography at 30 μM and 8 μM, respectively. SAH (Cat. A9384, Sigma-Aldrich, St. Louis, MO, USA) was included at 10 mM throughout purification to minimize conversion of endogenous PE to PMME.

For the $Cho2^{PMME}$ sample, 10 μM SAM (Cat. orb134825, Biorbyt, Cambridge, UK) was included throughout affinity purification, detergent exchange and size-exclusion chromatography. Following affinity purification, the eluate was supplemented with 0.1 mM SAM and incubated overnight before size-exclusion chromatography. Peak fractions were concentrated to 10.9 mg mL^{-1} and supplemented with 10 mM SAM and 0.1% digitonin immediately before vitrification. Inclusion of SAM throughout purification was intended to favor conversion of endogenous PE to PMME. In addition, 30 μM PMME (Cat. 850851P, Avanti Research, Alabaster, AL, USA) was supplied in the peak fractions from size exclusion chromatography before concentration.

For mutant assay, cell mass from 15 mL culture was re-suspended in 1 mL 1 mM dithiothreitol (DTT), 1 mM PMSF, 1 mM ethylenediaminetetraacetic acid (EDTA) in Buffer A and lysed using glass beads shaking at 8,000 rpm for 30 s with four cycles using a Precellys Evolution homogenizer (Bertin Technologies, Montigny-le-Bretonneux, France). The lysate was solubilized in 1 % DDM for 2 h. After centrifuging at 21,000 × g for 1 h, the supernatant fraction was mixed with 50 μL Streptactin beads for batch binding. The beads were harvested by centrifuging at 500 g for 1 min and washed once with 0.5 mL 0.03 % DDM, 0.2 mM TCEP, 1 M NaCl, 10 % glycerol, 50 mM Tris 8.0 and then twice with 0.5 mL 0.03 % DDM, 0.2 mM TCEP in Buffer A. The samples were eluted with 5 mM desthiobiotin, 0.03 % DDM, and 0.2 mM TCEP in

Buffer A. The protein concentration is determined using A493. The elution was aliquoted, snap-frozen in liquid nitrogen, and stored at -80 ℃ before use. Protein was quantified using absorbance at 493 nm with the theoretical extinction coefficient of 64,220 M^{-1} cm^{-1}.

Expression and purification – Fab8D3-2

The encoding sequence of the light chain and C terminal His-tagged heavy chain of Fab8D3-2[43] were cloned into pDEC vector[48]. Expi293 cells were transfected at a density of 2×10^6 cells mL^{-1} with equal amounts of the light- and heavy-chain plasmids (0.5 mg L^{-1} each) using linear polyethyleneimine (3 mg L^{-1}). Sodium butyrate was added to a final concentration of 10 mM 10–12 h after transfection to enhance protein expression. Cells were cultured for an additional 60 h before the conditioned medium was harvested by centrifugation and filtration through a 0.22-μm membrane. The clarified medium was adjusted to contain 5 mM imidazole, 150 mM NaCl, and 50 mM Tris-HCl pH 8.0 before incubation with Ni-Sepharose resin overnight at 4 °C. After washing with 20 CV of **Buffer C** (150 mM NaCl, 20 mM Tris-HCl, pH 8.0) containing 10 mM imidazole, Fab8D3-2 was eluted with **Buffer C** supplemented with 300 mM imidazole. Purified protein was aliquoted, flash-frozen in liquid nitrogen and stored at -80 °C. Protein was quantified using absorbance at 280 nm with the theoretical extinction coefficient of 80,385 M^{-1} cm^{-1}.

Expression and purification – MBP-PrA/G

The encoding sequence of MBP-PrA/G[43] with a C terminal 8 × His tag was cloned into the p3EC vector[49]. *Escherichia coli* BL21(DE3) cells carrying the plasmid were grown in Luria-Bertani (LB) medium medium containing 50 μg mL^{-1} kanamycin at 37 °C to an OD_{600} of approximately 0.6 before induction with 1 mM isopropyl β-D-thiogalactoside (IPTG) for 4 h. Cells were harvested, resuspended in **Buffer D** (400 mM NaCl, 20 mM imidazole, and 50 mM HEPES pH 7.5) supplemented with 5 mM $MgCl_2$, 10 μg mL^{-1} DNase I and 1 mM PMSF, and disrupted by high-pressure

769 homogenization. Following centrifugation at 25,000 × g for 30 min, the clarified lysate
770 was incubated with Ni-NTA resin for 3 h at 4 °C. After washing with 20 CV of Buffer
771 D, MBP-PrA/G was eluted with 300 mM imidazole, 150 mM NaCl, and 20 mM HEPES
772 pH 7.5. Protein was further purified by size-exclusion chromatography on a Superdex
773 200 Increase 10/300 GL column equilibrated in 5% (v/v) glycerol, 150 mM NaCl, and
774 20 mM HEPES pH 7.5. Peak fractions were aliquoted, flash-frozen in liquid nitrogen
775 and stored at -80 °C. Protein was quantified using absorbance at 280 nm with the
776 theoretical extinction coefficient of 77,810 M^{-1} cm^{-1}.
777
778 **Expression and purification – Nanobody**
779 The synthetic nanobody (Sybody) Sb26 was expressed with a C-terminally His-tag in
780 *E. coli* MC1061 cells. Cells carrying the pSb-init-Sb26 [42] plasmid were grown in
781 Terrific Broth supplemented with 25 μg mL^{-1} chloramphenicol at 37 °C to an OD_{600} of
782 approximately 0.5. Cultures were shifted to 22 °C for 1.5 h before protein expression
783 was induced with 0.02% (w/v) arabinose for 17 h. Periplasmic proteins were isolated
784 by osmotic shock. Briefly, cells from 1 L culture were resuspended in 20 mL TES-high
785 buffer (0.5 M sucrose, 0.5 mM EDTA, 0.2 M Tris-HCl pH 8.0) and incubated at 4 °C
786 for 30 min, followed by rapid dilution with 40 mL ice-cold Milli-Q water and
787 incubation for 1 h. The periplasmic extract was recovered by centrifugation at 25,000
788 × g for 30 min. The supernatant was adjusted to contain 20 mM imidazole, 150 mM
789 NaCl, and 2 mM $MgCl_2$ before incubation with Ni-NTA resin for 2 h. After washing
790 with 30 mM imidazole in 150 mM NaCl, and 20 mM Tris-HCl pH 8.0, Sb26 was eluted
791 with 300 mM imidazole in the buffer above. Purified protein was used immediately or
792 flash-frozen in liquid nitrogen and stored at -80 °C. Protein was quantified using
793 absorbance at 280 nm with the theoretical extinction coefficient of 44,015 M^{-1} cm^{-1}.
794
795 **Assembly of the Legobody complex**
796 The Legobody complex was assembled by mixing MBP-PrA/G, Fab8D3-2 and Sb26 at
797 a molar ratio of 1:1.1:3 and incubating the mixture on ice for 30 min. The assembled

complex was captured on amylose resin (Cat. E8021V, New England Biolabs) and washed with 6 CV of 150 mM NaCl, and 20 mM Tris-HCl pH 8.0 supplemented with 1 mM EDTA. The Legobody complex was eluted with 20 mM maltose in the buffer above.

Expression and purification – *Ct*Cho2 C^{sol}

Expression for *Ct*Cho2 C^{sol} was performed following the same procedure as for the full-length *Ct*Cho2. Cell pellets were cryogenically ground in a freezer mill (15 cycles s^{-1}, 25 cycles) and resuspended in Buffer A supplemented with 1 mM PMSF, 1 mM EDTA, and 0.2 mM TCEP. Cells were further disrupted using a high-pressure homogenizer (UH-06, Union, Shanghai, China) at 600–700 bar, and cell debris was removed by centrifugation at 30,000 × *g* for 30 min. The clarified lysate was incubated with 0.5 mL Strep-Tactin resin for 1 h at 4 °C. After washing with 10 CV of 0.2 mM TCEP in Buffer B, the resin-bound protein was incubated with preassembled Sb26 Legobody at a 1:2 molar ratio for 1 h. The resin was washed with 5 CV of 2 mM maltose, 0.2 mM TCEP, 150 mM NaCl, and 20 mM Tris-HCl pH 8.0. The *Ct*Cho2 C^{Sol}-Legobody complex was eluted with 5 mM D-desthiobiotinin. The complex was further purified by size-exclusion chromatography on a Superose 6 Increase 10/300 GL column equilibrated with 2 mM maltose, 0.2 mM TCEP, 150 mM NaCl, and 20 mM Tris-HCl pH 8.0. Peak fractions were pooled, concentrated to 6.4 mg mL^{-1}, and used for cryo-EM. Protein was quantified using absorbance at 280 nm with the theoretical extinction coefficient of 64,220 M^{-1} cm^{-1}.

Sybody selection

Avi-tagged *Ct*Cho2 was purified in GDN as described above and exchanged into0.008 % GDN, 0.2 mM TCEP in Buffer A using a desalting column (Cat. 732-2010, Bio-Rad, Hercules, CA, USA). For simultaneous tag removal and biotinylation, purified *Ct*Cho2 (2 mg mL^{-1}) was incubated overnight at 4 °C with 3C protease (34 μg mL^{-1}), BirA ligase (24 μg mL^{-1})[50], 10 mM magnesium acetate, 5 mM ATP, and 20 μM biotin. After reverse

Ni-NTA purification to remove the cleaved TGP tag and BirA, biotinylated *Ct*Cho2 was further purified by Superdex 200 Increase 10/300 GL chromatography in 0.008% GDN, 10% glycerol, 150 mM NaCl, and 20 mM Tris-HCl pH 8.0. Peak fractions were concentrated, aliquoted, flash-frozen, and stored at -80 °C. Sybody screening was performed as described[42] using one round of ribosome display followed by three rounds of phage display. Briefly, an *in vitro* translation reaction mixture (4 µL of solution I, 0.5 µL of solution II, 1 µL of solution III, 0.5 µL of 10 mM cysteine, 0.5 µL of 80 mM reduced glutathione, 0.5 µL of 60 mM oxidized glutathione, 0.5 µL of 1.875 mg mL^{-1} disulfide bond isomerase DsbC and 1.8 µL of nuclease-free water) was incubate for 5 minutes at 37°C in a PCR cycler. Sybody mRNA-libraries[42] was added to the mixture and the reaction was proceeded for 30 minutes at 37°C to form translation complexes. The reaction mix was then diluted into the 100 µL ice cold panning solutions (50 mM Tris-acetate, 150 mM NaCl, 50 mM magnesium acetate, 0.5 % bovine serum albumin (BSA), 0.1 % GDN, Heparin stock solution, RnaseIn) and centrifuged at 20,000 × g for 5 minutes at 4°C. Biotinylated *Ct*Cho2 was added to the supernatant to a final concentration of 50 nM and incubate on ice for 20 min for solution panning. Sybody binders were pulled down using 12 µl pre-washed and blocked streptavidin beads (Dynabeads Myone Streptavitin T1). After washing trice with 500 µl ice cold WTB-D (50 mM Tris acetate, 150 mM NaCl, 50 mM magnesium acetate, 0.008 % GDN), mRNA were eluted using yeast RNA and EDTA, purified using the RNeasy micro kit and reverse transcribed into cDNA. The resulting cDNA was purified using a DNA Purification kit (Cat. 740609, Macherey-Nagel, Düren, Germany), amplified using respect primer, and ligated into pDX-init vector after *BspQ*I digestion. The ligation product was transformed into *E. coli* SS320 cells using electric transportation to generate phage library. Three rounds of phage display were subsequently performed with increasing selection stringency. The first round used neutravidin-coated plates with 50 nM biotinylated *Ct*Cho2. The second and third rounds employed MyOne Streptavidin C1 beads together with off-rate selection by competition with excess non-biotinylated *Ct*Cho2 (5 µM and 0.5 µM, respectively), while reducing the concentration of biotinylated *Ct*Cho2 to 5 nM in the final round. Selected phagemids were subcloned

into pSb_init by FX cloning for expression in *E. coli* MC1061.

Single colony enzyme-linked immunosorbent assay (ELISA)

Individual MC1061 colonies expressing Myc-tagged sybodies were grown in Terrific Broth containing 25 μg mL^{-1} chloramphenicol and induced with 0.02% (w/v) arabinose at 22 °C overnight. Periplasmic extracts were prepared by osmotic shock using TES buffer (0.5 mM EDTA, 0.5 μg/mL lysozyme, 20% (w/v) sucrose, 50 mM Tris-HCl pH 8.0) followed by dilution into Buffer B supplemented with 1 mM $MgCl_2$. ELISA screening was performed essentially as described previously[50] except that 0.008 %(w/v) GDN was included in all buffers. MaxiSorp plates were coated with Protein A overnight at 4 °C, blocked with 0.5% BSA, and sequentially incubated with anti-Myc antibody, periplasmic extracts, and 50 nM biotinylated *Ct*Cho2 (or an unrelated membrane protein as a specificity control). Bound antigen was detected using streptavidin-horseradish peroxidase (HRP) and 3,3',5,5'-tetramethylbenzidine (TMB) substrate, and absorbance at 650 nm was measured using a SpectraMax M2e plate reader (Molecular Devices, San Jose, CA, USA).

Activity assay

POPE (Cat. 850757P, Avanti Research, Alabaster, AL, USA) dissolved in chloroform was dried under argon and further lyophilized under high vacuum (Model Model FreeZone 2.5L, Labconco, Kansas City, MO, USA) for 4 h. The dried lipid film was resuspended by sonication for 15 min in 1 mM Triton X-100 (Cat. X-100, Sigma, St. Louis, MO, USA), 1 mM EDTA, 0.4 mM TCEP, 50 mM Tris-HCl pH 9.2 to generate a 4-mM stock (80 mol % relating to Triton X-100). Enzymatic assay was performed in a 1.5-mL Eppendorf tube with a final volume of 20 μL containing 2 mM POPE, 1 mM SAM (specific activity 3 mCi $mmol^{-1}$ after dilution of [^{3}H]-SAM with unlabeled SAM), 10 μg mL^{-1} purified *Ct*Cho2, and 50 mM glycine (pH 9.0). Reactions were initiated by addition of SAM and incubated at 25 °C for 30 min, during which time window the enzyme activity was linear with time and enzyme loading (0.5-20 μg mL^{-1}). Reactions were terminated by adding 200 μL chloroform:methanol (1:1, v/v), followed by 500 μL

887 water. After vortexing for 1 min and centrifugation at 12,000 × *g* for 2 min, the aqueous
888 phase was discarded and the organic phase was washed twice with water. The organic
889 solvent was evaporated, and the remaining lipids were resuspended in 500 µL
890 scintillation cocktail (Cat. 1200.437, Revvity, Waltham, MA, USA). Radioactivity was
891 measured using a Tri-Carb 5110TR liquid scintillation counter (PerkinElmer, Shelton,
892 CT, USA). For determination of the apparent K_m for SAM, reactions contained 0.03–2
893 mM SAM, 2 mM POPE, and 1 µg mL^{-1} purified *Ct*Cho2. Michaelis-Menten parameters
894 were obtained by nonlinear regression using GraphPad Prism 9. For inhibition assays,
895 reactions contained 2 mM POPE, 5 mM SAM, 20 µg mL^{-1} *Ct*Cho2, and 50 mM glycine
896 (pH 9.0). A stock solution of 1-palmitoyl-2-oleoyl-*sn*-glycero-3-phosphocholine
897 (POPC; Cat. A80557, Avanti Polar Lipids) was prepared as described above for POPE.
898 Phosphatidylserine (PS) was included as a control, with its concentration adjusted to
899 maintain a constant total phospholipid molar percentage across conditions and thereby
900 minimize potential effects arising from changes in the micellar environment.
901
902 **Cryo-EM sample preparation**
903 Purified *Ct*Cho2 samples (2.5 µL) were applied onto a glow-discharged Quantifoil Au
904 R1.2/1.3 (300 mesh) grid. The grid was blotted for 4 s with a blot force of 0 at 8 °C
905 under 100% humidity using a Mark IV Vitrobot machine (FEI). After blotting, the grid
906 was flash-frozen by plunging into liquid ethane.
907
908 **Cryo-EM data collection**
909 Cryo-EM data of Cho2$^{PE/PC}$ were collected using a 300 keV Krios G4 cryo-electron
910 microscope (Thermo Fisher Scientific, Waltham, MA, USA) equipped with a Falcon 4i
911 direct electron detector, a Selectris X energy filter operated at an 8-eV slit width, and a
912 Spherical Aberration Corrector. Images were acquired using EPU (v3.8.1), with two
913 exposures per hole, at magnifications listed in **Table S1**. Data for Cho2^{PE} and Cho2^{PMME}
914 were collected using Titan Krios G4 cryo-electron microscope equipped with a Falcon
915 G4i detector, a Selectris X energy filter operated at a 20-eV slit width. Data for C^{Sol}
916 were collected on a 200 kV Glacios 2 cryo-electron microscope (Thermo Scientific)

equipped with a Falcon 4i direct electron detector.

Data were processed using cryoSPARC (v4.7.1)[51]. Briefly, after motion correction and CTF refinement, particles were blob picked and extracted with a box size of 384 pixels and Fourier crop to box size of 120 pixels. The particles were subjected to rounds of 2D classification and heterogeneous refinement. The 'good'[52] particles were used as template for Topaz training[52]. The Topaz extracted particles were subjected to multiple rounds of 2D classification, heterogeneous refinement, rebalance orientation, subset particles, and manual removal, to improve orientation distribution. After global CTF refinement, reference-based motion correction and non-uniform refinement, the particles were subjected to local refinement with C2 symmetry. The resolution of the map was estimated using gold-standard FSC with a threshold of 0.143. Data processing pipelines were individually summarized in **Fig. S3, S5-S7** and **Table S1**.

Model building and molecular docking

Models were built manually using Coot (v0.9.6)[53] and refined using Phenix (v1.19.2)[54]. Molecular docking was performed using AutoDock 4.0 (Schrödinger)[55]. Structures were visualized using ChimeraX (v1.11)[56].

DATA AVAILABILITY

The coordinates for the models and the cryo-EM maps generated in this study have been deposited in the PDB and EMDB under the following accession codes: $Cho2^{PE/PC}$, 44KX and EMD-82678; $Cho2^{PE}$, 44KW and EMD-82677; $Cho2^{PMME}$, 44KU and EMD-82675; C^{Sol}, 44KV and EMD-82676.

ACKNOWLEDGEMENTS

We thank the staff members of the Center of Cryo-EM of Sun Yat-sen University, Core Facilities of Molecular Biology and Cell Biology in Shanghai Institute of Biochemistry and Cell Biology, the Center of Cryo-EM of Fudan University, and the Shenzhen

Medical Academy of Research and Translation (SMART) for technical assistance. We thank Prof. Lilin Du and Dr. Xiaoran Zhang at National Institute of Biological Sciences (Beijing, China) for providing strains, plasmids, protocols and guidance for *S. pombe* genetic manipulations. This work has been supported by the National Natural Science Foundation of China (32571459, T.L., 32471246 & W2412096, D.L.; 82521001 & 32371256, Q.Q.), the National Key Research and Development Program of China (2023YFA0915000) and the start-up funds from Sun Yat-sen University.

AUTHOR CONTRIBUTIONS

T.L. and H.X. purified and characterized enzyme. T.L. H.X. and Y.C. prepared grids. T.L. and Y.C. collected cryo-EM data with assistance from Z.Z.. T.L., Q.Q., and D.L. processed cryoEM data. Y.L. performed molecular docking. D.L. oversaw the project. D.L. wrote the manuscript with inputs from T.L., H.X., Z.Y., and Q.Q.

COMPETING INTERESTS STATEMENT

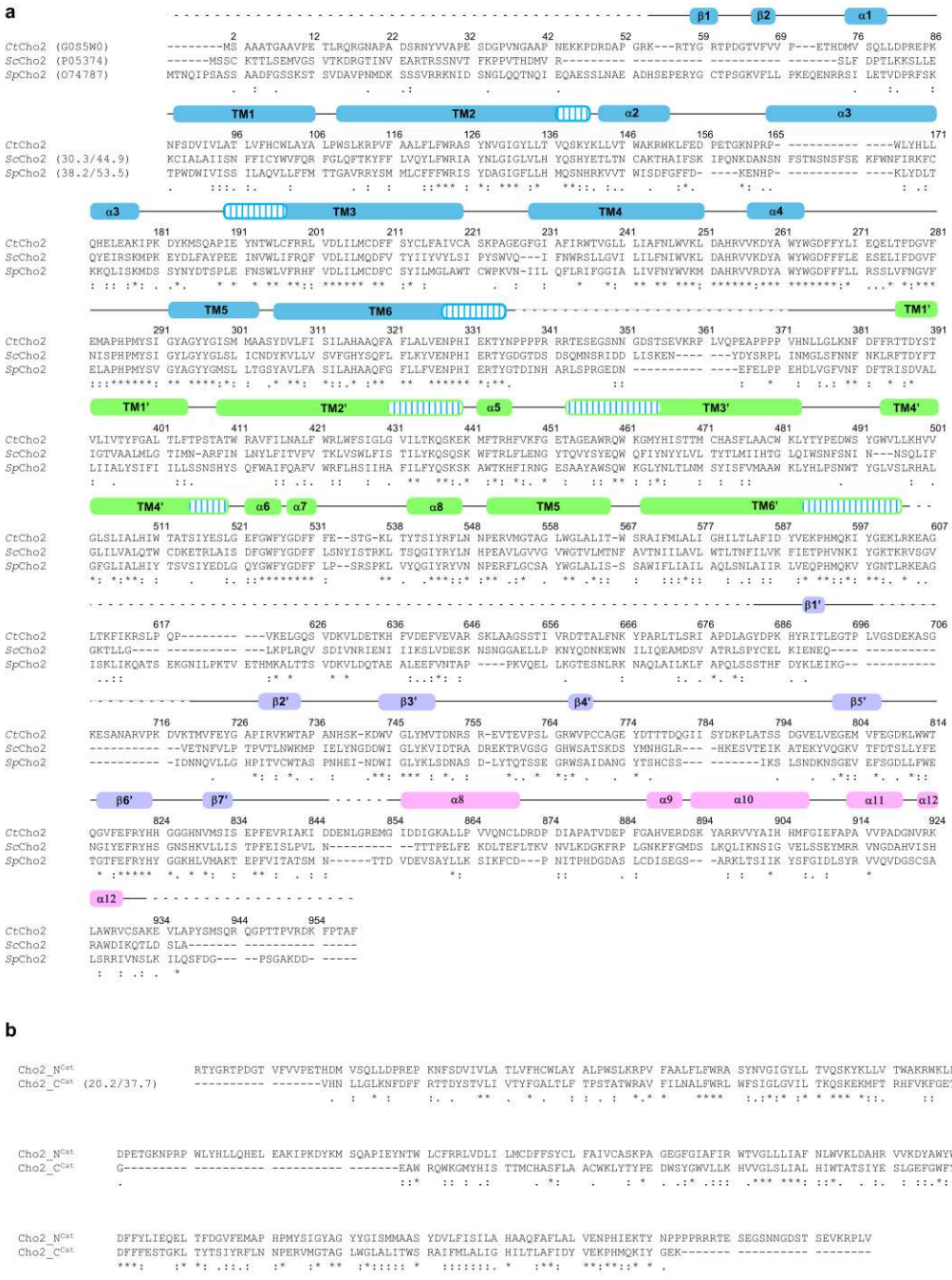
The authors declare no competing interests.

Supplementary Information

Supplementary Fig. 1-8

Supplementary Table 1

Still image and caption for Movie 1



969

970 **Fig. S1 | Sequence analysis of Cho2. a** Sequence alignment of Cho2 from *Chaetomium*
971 *thermophilum* (*Ct*Cho2, Uniprot ID G0S5W0), *Saccharomyces cerevisiae* (*Sc*Cho2,
972 Uniprot ID P05374) and Shinzosaccharomyces pombe (*Sp*Cho2, Uniprot ID O74787).
973 Asterisk, colon, and dot indicate identical, conserved, and semi-conserved substitutions,
974 respectively. Secondary structure segments are numbered in accord with **Fig. 2c, 2d,**
975 **and 5a**. Sequence identity/similarity (%) to *Ct*Cho2 are shown in brackets. **b** Sequence
976 alignment of the N-terminal catalytic domain (N^{Cat}) with C^{Cat}. Sequence
977 identity/similarity (%) between the two domains are shown in brackets.

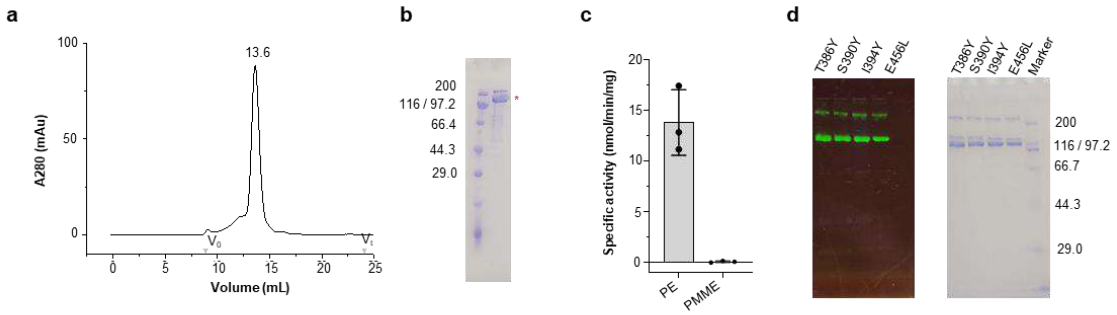


Fig. S2 | Purification and enzymatic characterization of *Ct*Cho2 and mutants. a,b Size exclusion chromatography (**a**) and SDS-PAGE (**b**) of wild-type *Ct*Cho2. **c** Substrate specificity of *Ct*Cho2. PE, phosphatidylethanolamine; PMME, phosphatidyl monomethylethanolamine. **d** SDS-PAGE of dimer-interface mutants. Protein bands were visualized by TGP in-gel fluorescence (left) or Coomassie Blue staining (right).

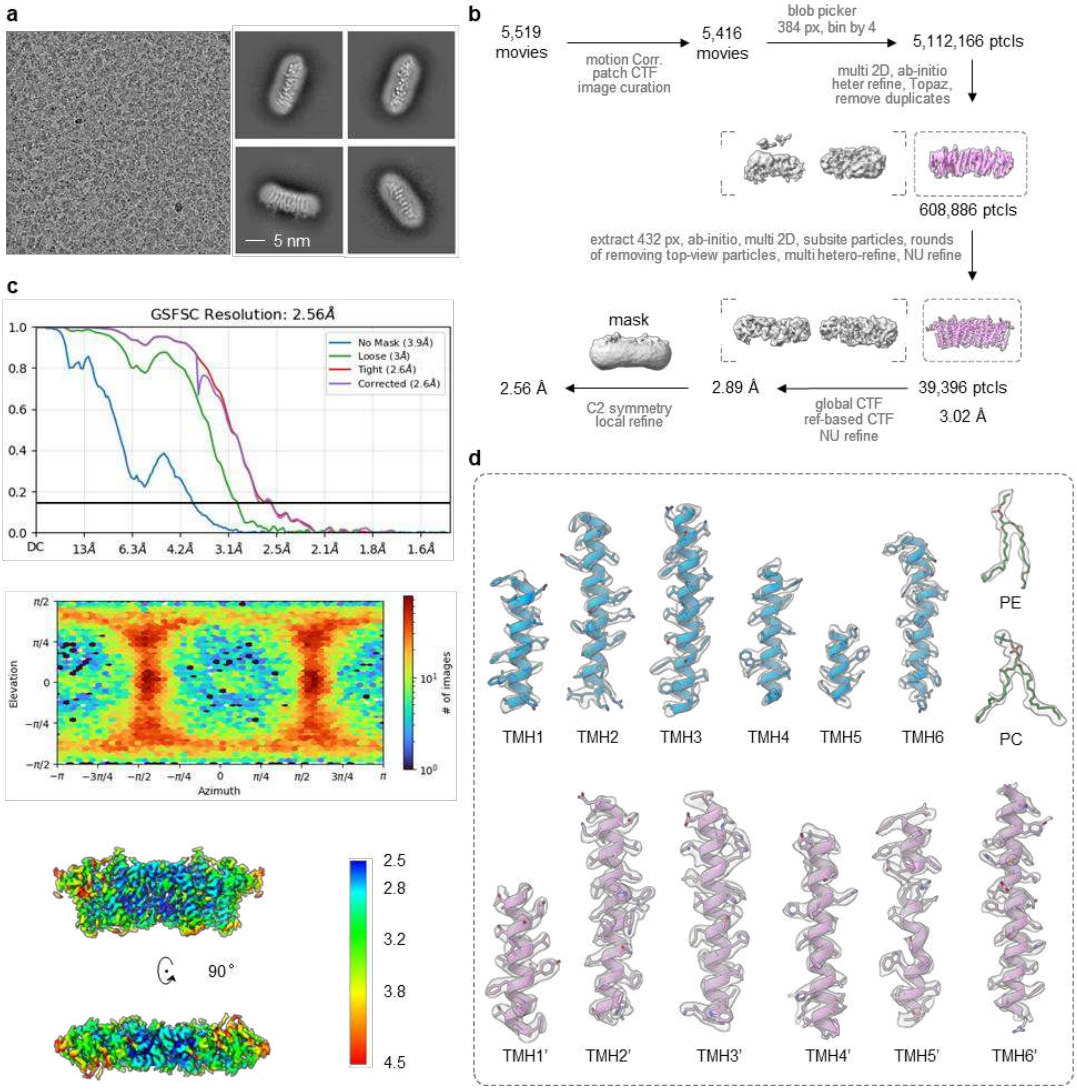


Fig. S3 | Cryo-EM analysis of *Ct*Cho2$^{PE/PC}$. a Representative micrograph and selected 2D class averages. **b** Workflow of particle classification and refinement. **c** Resolution assessment. Top, the nominal resolution by the 'gold-standard' Fourier shell correlation (FSC = 0.143); middle, angular distribution; bottom, local resolution map. **d** Representative density and model for transmembrane helices and the two active site lipids, phosphatidylethanolamine (PE) and phosphatidylcholine (PC).

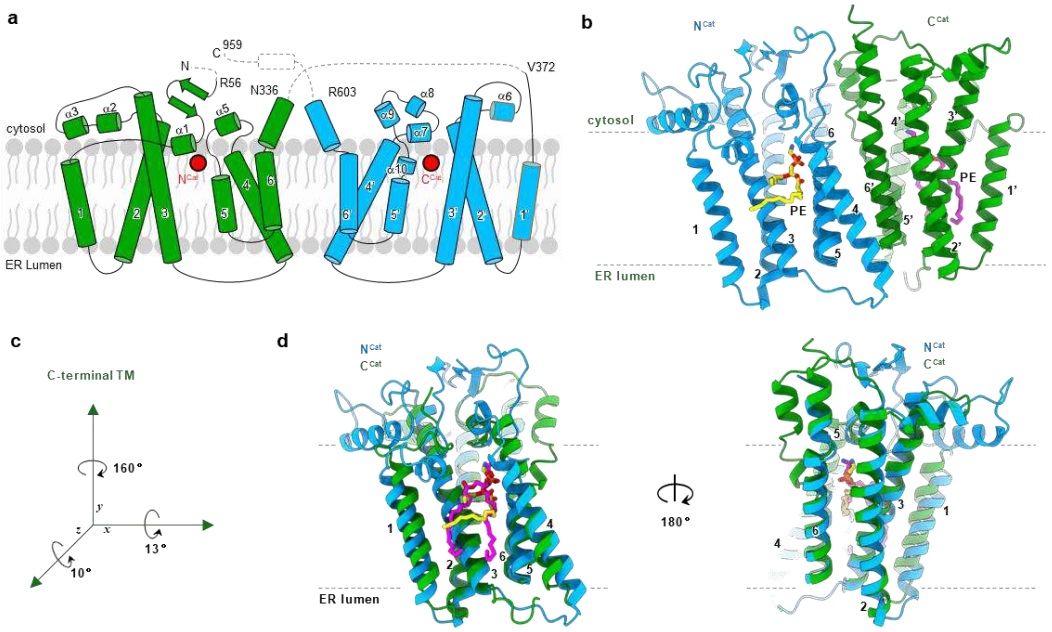
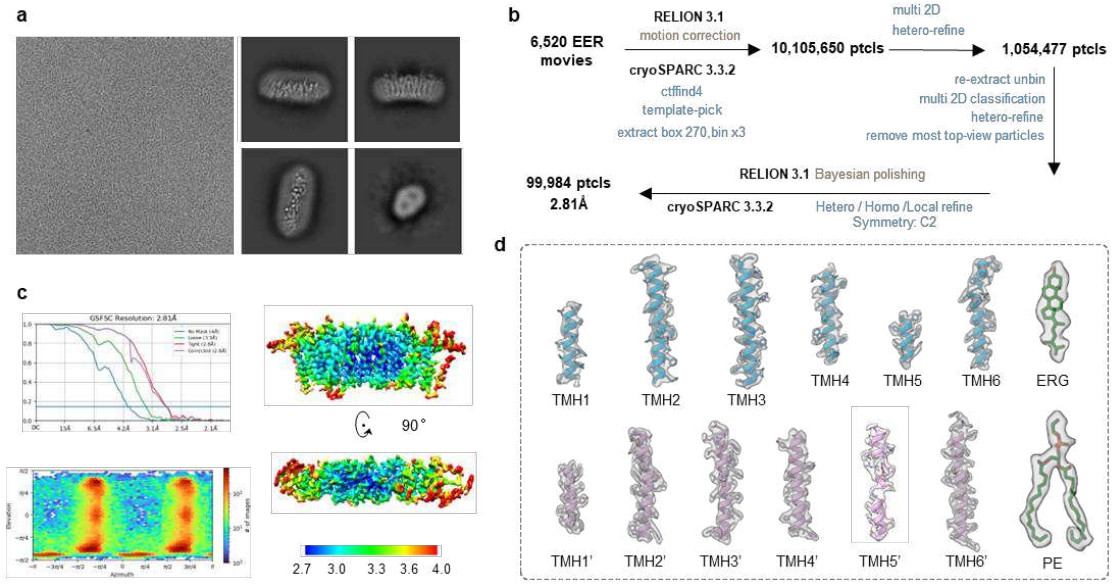


Fig. S4 | Pseudo-symmetry of the catalytic domains. a Membrane topology of *Ct*Cho2. **b** Structure of a *Ct*Cho2 protomer. **c** Relative orientation of the NCat and CCat domains. **d** Structural superposition of N^{Cat} and C^{Cat}. TMHs are numbered 1–6 in N^{Cat} and 1'–6' in C^{Cat} to reflect their pseudo-symmetrical relationship.



998

999

1000 **Fig. S5 | Cryo-EM data processing for *Ct*Cho2^{PE}. a** Representative micrograph and
1001 selected 2D class averages. **b** Workflow of particle classification and refinement. **c**
1002 Resolution assessment. Top, the nominal resolution by the 'gold-standard' Fourier shell
1003 correlation (FSC = 0.143); middle, angular distribution; bottom, local resolution map.
1004 **d** Representative density and model for transmembrane helices and the
1005 phosphatidylethanolamine (PE) molecules at the two active sites.

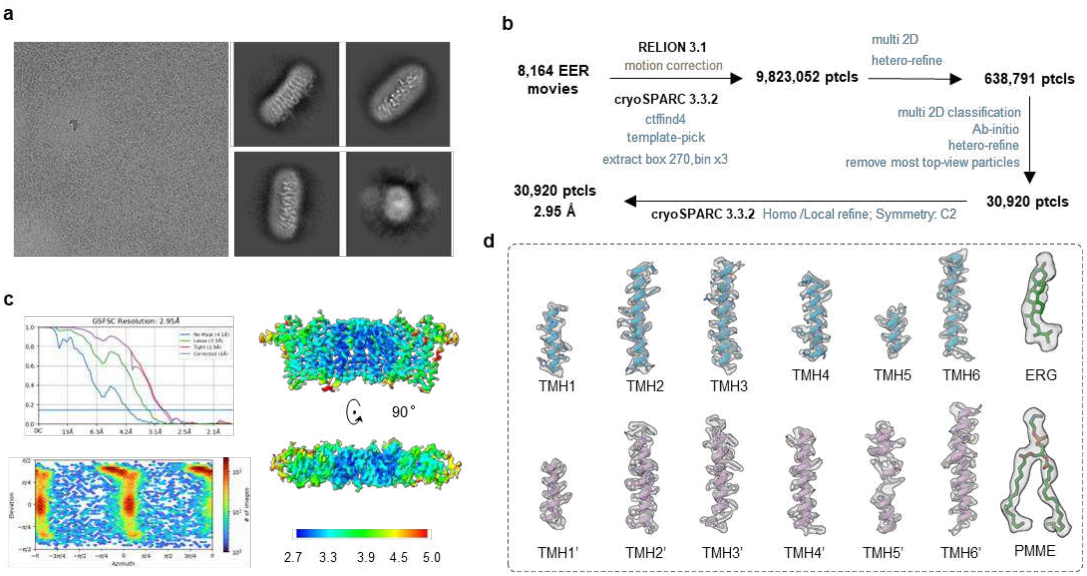


Fig. S6 | Cryo-EM data processing for *Ct*Cho2^{PMME}. a Representative micrograph and selected 2D class averages. **b** Workflow of particle classification and refinement. **c** Resolution assessment. Top, the nominal resolution by the 'gold-standard' Fourier shell correlation (FSC = 0.143); middle, angular distribution; bottom, local resolution map. **d** Representative density and model for transmembrane helices and the phosphatidylmonomethylethanolamine (PMME) molecules at the two active sites.

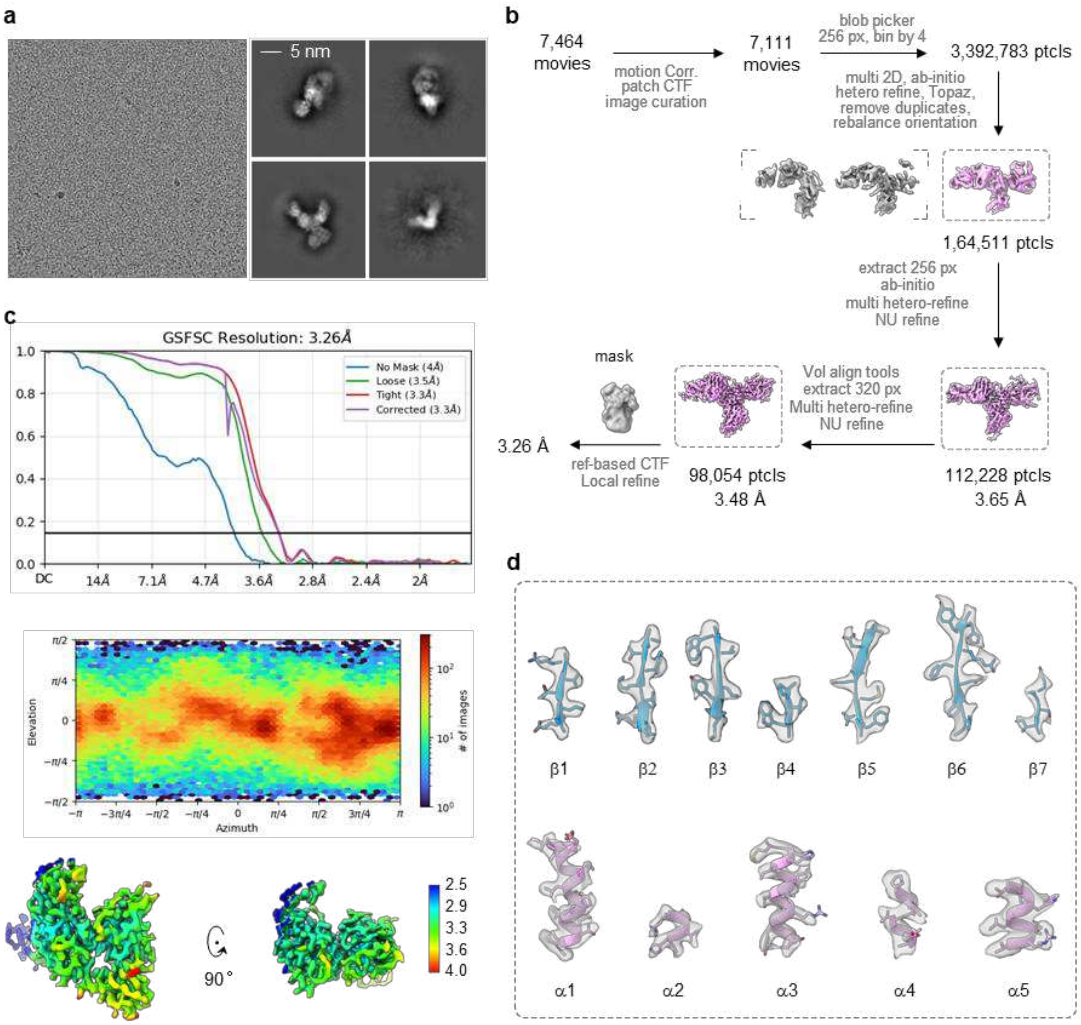


Fig. S7 | Cryo-EM data processing for *Ct*Cho2 C^{Sol}. a Representative micrograph and selected 2D class averages. **b** Workflow of particle classification and refinement. **c** Resolution assessment. Top, the nominal resolution by the 'gold-standard' Fourier shell correlation (FSC = 0.143); middle, angular distribution; bottom, local resolution map. **d** Representative density and model for α-helices and β-strands.

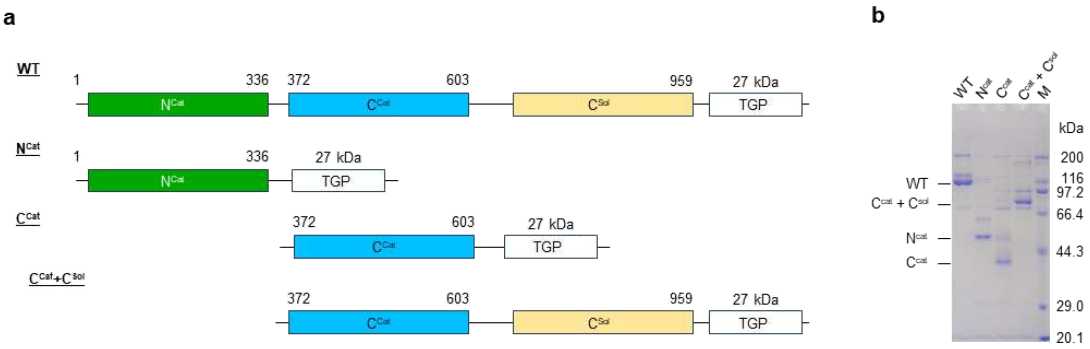
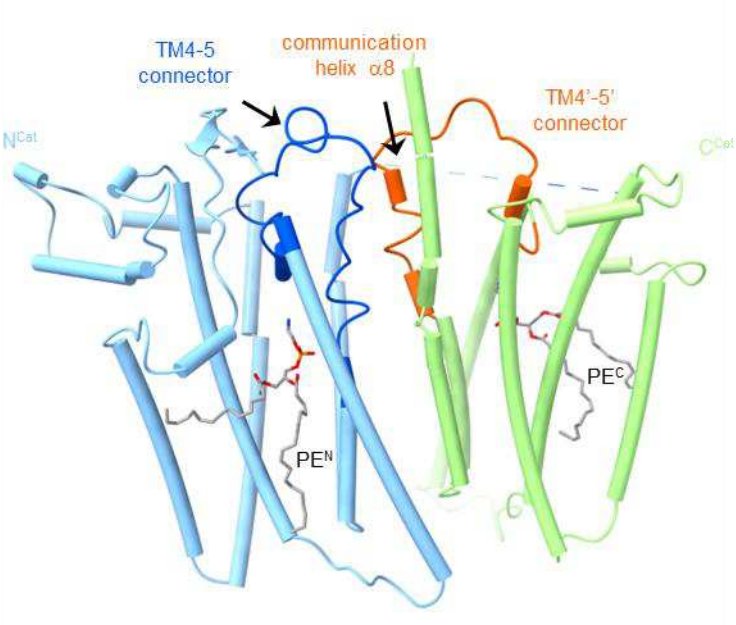


Fig. S8 | Purification of truncation mutants. a Schematic representation of the truncation constructs. **b** SDS-PAGE analysis of purified truncation mutants.



Movie 1 | Conformational transition between the SAM-free and SAM-bound states. The SAM-free state was represented by the *Ct*Cho2^{PE} structure, whereas the SAM-bound state was generated by docking SAM into a SWISS-MODEL homology model of CtCho2 using the human PEMT structure (PDB 44UN) as the template. The molecular morph was generated using ChimeraX, with relevant structural elements labeled accordingly.

1033 **Table S1. Cryo-EM data collection and refinement statistics.**

	*Ct*Cho2$^{PE/PC}$	*Ct*Cho2^{PE}	*Ct*Cho2^{PMME}	*Ct*Cho2-C^{sol}
Data collection				
Magnification	130 k	130 k	130 k	150k
Voltage (kV)	300	300	300	200
Electron exposure ($e^-/Å^2$)	50	50	50	50
Defocus range (μm)	-2.2 to -1.2	-2.0 to -1.5	-2.0 to -1.5	-2.2 to -1.2
Pixel size (Å)	0.728	0.932	0.932	0.89
Symmetry imposed	C2	C2	C2	C1
Initial particle images (No.)	5,112,166	10,105,650	9,823,052	3,392,783
Final particle images (No.)	39,050	99,984	30,920	98,054
Map resolution (Å)	2.56	2.81	2.95	3.26
FSC threshold	0.143	0.143	0.143	0.143
Refinement				
Model resolution (Å)	3.0	3.3	3.4	3.6
FSC threshold	0.5	0.5	0.5	0.5
Map sharpening *B* factor ($Å^2$)	-45.5	-81.9	-60.8	-123.3
Model composition				
Non-hydrogen atoms	10,017	8,952	8,286	2,678
Protein residues	1,034	1,026	1,028	338
Ligands / ion	64	22	6	0
B factor ($Å^2$)				
Protein	112.71	97.58	68.59	40.77
Ligand	133.36	97.66	59.09	-
R.m.s. deviations				
Bond lengths (Å)	0.006	0.011	0.012	0.005
Bond angles (°)	0.792	1.037	1.437	0.761
Validation				
MolProbity score	2.12	2.31	3.14	2.33
Clashscore	13.29	10.24	32.94	22.54
Ramachandran plot				
Favored (%)	98.25	97.45	97.25	96.97
Allowed (%)	1.75	2.55	2.75	3.03
Outliers (%)	0.00	0.00	0.00	0.00

1034

Supplementary Files

This is a list of supplementary files associated with this preprint. Click to download.

- Cho2.mp4